AGU ADVANCING EARTH AND SPACE SCIENCES

AGU Advances

RESEARCH ARTICLE
10.1029/2023AV000870

Multi-Layer Evolution of Acoustic-Gravity Waves and Ionospheric Disturbances Over the United States After the 2022 Hunga Tonga Volcano Eruption

P. A. Inchin[1], A. Bhatt[2], S. A. Cummer[3], S. D. Eckermann[4], B. J. Harding[5], D. D. Kuhl[6], J. Ma[4], J. J. Makela[7], R. Sabatini[1], and J. B. Snively[1]

[1]Department of Physical Sciences and Center for Space and Atmospheric Research, Embry-Riddle Aeronautical University, Daytona Beach, FL, USA, [2]SRI International, Menlo Park, CA, USA, [3]Duke University, Durham, NC, USA, [4]Space Science Division, U.S. Naval Research Laboratory, Washington, DC, USA, [5]Space Sciences Laboratory, University of California Berkeley, Berkeley, CA, USA, [6]Remote Sensing Division, U.S. Naval Research Laboratory, Washington, DC, USA, [7]Department of Electrical and Computer Engineering, University of Illinois Urbana-Champaign, Urbana, IL, USA

Peer Review The peer review history for this article is available as a PDF in the Supporting Information.

Key Points:

- The atmosphere and ionosphere exhibited propagating acoustic-gravity waves (AGWs) and traveling ionospheric disturbances (TIDs) over CONUS that accompanied the arrivals of Lamb wave modes
- Independent confirmations of packets of AGWs and TIDs are consistent with at least 4 sets of eruption-related events
- The importance of atmospheric state and winds on Lamb wave mode propagation is demonstrated with ray-tracing modeling results

Supporting Information:

Supporting Information may be found in the online version of this article.

Correspondence to:

P. A. Inchin,
inchinp@erau.edu

Citation:

Inchin, P. A., Bhatt, A., Cummer, S. A., Eckermann, S. D., Harding, B. J., Kuhl, D. D., et al. (2023). Multi-layer evolution of acoustic-gravity waves and ionospheric disturbances over the United States after the 2022 Hunga Tonga volcano eruption. *AGU Advances*, *4*, e2023AV000870. https://doi.org/10.1029/2023AV000870

Received 18 JAN 2023
Accepted 26 OCT 2023

Author Contributions:

Conceptualization: P. A. Inchin, R. Sabatini, J. B. Snively
Data curation: P. A. Inchin, A. Bhatt, S. A. Cummer, S. D. Eckermann, B. J. Harding, D. D. Kuhl, J. Ma, J. J. Makela

Abstract The Hunga-Tonga Hunga-Ha'apai volcano underwent a series of large-magnitude eruptions that generated broad spectra of mechanical waves in the atmosphere. We investigate the spatial and temporal evolutions of fluctuations driven by atmospheric acoustic-gravity waves (AGWs) and, in particular, the Lamb wave modes in high spatial resolution data sets measured over the Continental United States (CONUS), complemented with data over the Americas and the Pacific. Along with >800 barometer sites, tropospheric observations, and Total Electron Content data from >3,000 receivers, we report detections of volcano-induced AGWs in mesopause and ionosphere-thermosphere airglow imagery and Fabry-Perot interferometry. We also report unique AGW signatures in the ionospheric D-region, measured using Long-Range Navigation pulsed low-frequency transmitter signals. Although we observed fluctuations over a wide range of periods and speeds, we identify Lamb wave modes exhibiting 295–345 m s^{-1} phase front velocities with correlated spatial variability of their amplitudes from the Earth's surface to the ionosphere. Results suggest that the Lamb wave modes, tracked by our ray-tracing modeling results, were accompanied by deep fluctuation fields coupled throughout the atmosphere, and were all largely consistent in arrival times with the sequence of eruptions over 8 hr. The ray results also highlight the importance of winds in reducing wave amplitudes at CONUS midlatitudes. The ability to identify and interpret Lamb wave modes and accompanying fluctuations on the basis of arrival times and speeds, despite complexity in their spectra and modulations by the inhomogeneous atmosphere, suggests opportunities for analysis and modeling to understand their signals to constrain features of hazardous events.

Plain Language Summary The 2022 eruption of the Hunga Tonga–Hunga Ha'apai volcano launched waves of exceptional strength—extending to space, into the thermosphere and ionosphere (~300 km height)—that traveled across the globe over the course of several days. We present an analysis of observations of waves and their effects over the Continental United States, using high-resolution data sets from Earth's surface to the ionosphere. Results include joint analysis of surface pressure and tropospheric fluctuations, imagery of waves in mesospheric and ionospheric airglow, data from a unique lower-ionospheric radio remote sensing experiment, as well as mapping of ionospheric fluctuations with networks of Global Navigation Satellite System receivers. Multi-layer/multi-instrument measurements show different fluctuation characteristics at different altitudes, but consistency in their initial arrival times and amplitude inhomogeneity with the Lamb wave modes measured in the lower atmosphere. Lamb wave modes are additionally investigated through ray-tracing modeling to track their propagation over Continental United States (CONUS). Back-tracing results also suggest the consistency of fluctuation arrivals to CONUS with a sequence of four events. These efforts point to strategies and applications for future observations and modeling, toward understanding the details of natural and anthropogenic hazard processes from the waves that they launch from Earth's surface to space.

1. Introduction

Natural hazards (NHs) can be sources of propagating waves in fluids and solid media of the Earth. The characteristics of waves provide important information about their sources, such as generation mechanisms, magnitudes, locations, time evolutions, and anisotropies. Source-inferring techniques allow investigations of earthquakes

Formal analysis: P. A. Inchin, A. Bhatt, S. A. Cummer, S. D. Eckermann, B. J. Harding, D. D. Kuhl, J. Ma, J. J. Makela, R. Sabatini
Funding acquisition: J. B. Snively
Investigation: P. A. Inchin, A. Bhatt, S. A. Cummer, S. D. Eckermann, B. J. Harding, D. D. Kuhl, J. Ma, J. J. Makela, R. Sabatini
Methodology: P. A. Inchin, A. Bhatt, S. A. Cummer, S. D. Eckermann, B. J. Harding, D. D. Kuhl, J. Ma, J. J. Makela, R. Sabatini, J. B. Snively
Project Administration: J. B. Snively
Resources: A. Bhatt, S. A. Cummer, J. J. Makela, R. Sabatini, J. B. Snively
Software: P. A. Inchin, A. Bhatt, S. D. Eckermann, D. D. Kuhl, J. Ma, R. Sabatini
Supervision: P. A. Inchin, J. B. Snively
Validation: P. A. Inchin, A. Bhatt, S. A. Cummer, S. D. Eckermann, B. J. Harding, D. D. Kuhl, J. Ma, J. J. Makela, R. Sabatini
Visualization: P. A. Inchin, A. Bhatt, B. J. Harding
Writing – original draft: P. A. Inchin, A. Bhatt, S. A. Cummer, B. J. Harding, J. J. Makela, R. Sabatini, J. B. Snively
Writing – review & editing: P. A. Inchin, A. Bhatt, S. A. Cummer, S. D. Eckermann, B. J. Harding, D. D. Kuhl, J. Ma, J. J. Makela, R. Sabatini, J. B. Snively

and volcanic eruptions (Ji et al., 2002; Kanamori & Given, 1981; Ohminato et al., 1998), tsunamis (Gusman et al., 2014; Titov et al., 2005), meteorological events (Shao & Lay, 2016), explosions and nuclear tests (Assink et al., 2016; Pilger et al., 2021), and large meteors and bolides (Brown et al., 2002; Edwards & Hildebrand, 2004). The robustness and accuracy of these techniques depend on the quality and coverage of measurements and the suitability of instrumentation.

Along with propagation in the media in which the waves are generated, the continuity of dynamics across boundaries between Earth's fluid envelopes (e.g., ocean and atmosphere), and the subsequent transfer of momentum and energy between them, suggest opportunities to diagnose waves occurring in one medium through observations of their impacts in others. An important line of investigation is the study of the upward evolutions of NH-generated waves in the atmosphere and their observable impacts on the ionosphere (Astafyeva & Shults, 2019; Komjathy et al., 2016; Pilger et al., 2021), as measured by a variety of instruments at ground or in space, remotely or in-situ (Assink et al., 2012; Azeem et al., 2015; Makela et al., 2011; Nishioka et al., 2013; Taylor & Hapgood, 1988). Such studies are necessary steps toward incorporating NH-related atmospheric wave measurements into assessments of their sources: for example, localization, and constraining the severity or evolution of NHs (e.g., Inchin et al., 2021; Rakoto et al., 2018; Zedek et al., 2021). At the same time, analyzing atmospheric waves, which are often nonlinear, requires thorough understanding of their propagation and evolution through real environments, the mechanisms of their excitation and coupling with Earth's interior and oceans, as well as the uncertainties of observations thereof. The understanding of their dynamics leads to improved monitoring, diagnostics, and mitigation of risks to society and systems (Paxton et al., 2022; Zawdie et al., 2022), raising the possibility of eventually using atmospheric wave observations to supplement NH early-warning systems (Le Pichon et al., 2021; Martire et al., 2023; Savastano et al., 2017).

In our following discussion of observed fluctuations induced by the Hunga Tonga-Hunga Ha'apai volcano eruption in 2022, we introduce the terminology of *acoustic-gravity waves (AGWs)* to describe the spectrum of mechanical waves arising from the compressibility and buoyant stratification of the atmosphere (e.g., Francis, 1973; Godin, 2012; Hines, 1960; Press & Harkrider, 1962). In the framework of this manuscript, we consider the range from infrasonic (acoustic) waves of frequencies <20 Hz, propagating as compressions of the atmospheric gas, to gravity waves of tens of minutes of periods due to buoyant oscillations, with wave modes between exhibiting both phenomena (Press & Harkrider, 1962), such as AGWs that extend through many atmospheric scale heights. In the context of this study, it is important to highlight a mode that marks the boundary between acoustic and gravity wave dynamics, called the Lamb wave. In its classical derivation for an isothermal windless atmosphere, the Lamb wave is a compressional mode that propagates horizontally and non-dispersively with a speed of sound and exhibits exponential decay of wave energy density with height (Lamb, 1924). Wave modes similar to Lamb's classical solution also arise in real atmospheres (Bretherton, 1969; Garrett, 1969; Lindzen & Blake, 1972; C. H. Liu et al., 1982; Peltier & Hines, 1976) and so, to simplify our terminology, we will refer to them as just *Lamb wave modes*.

We note that our study is devoted to the investigation of fluctuations in the atmosphere and ionosphere generated by the spectrum of waves primarily timed with the Lamb wave, originating from multiple source processes associated with this volcanic eruption of rare magnitude. The wave spectrum of interest includes AGW modes of propagation—for example, infrasound/acoustic waves, Lamb waves, shorter-period gravity waves, and evanescent fluctuations, as well as resonances and ducted modes. We want to highlight their specific underlying physical nature as wave motions that emerge in a compressible atmosphere, with emphasis on the prominent signals observed to arrive over the US with the Lamb (acoustic) wave at similar propagation speed over multiple altitudes. These waves fall into this overarching definition of AGWs. Similarly, we will refer to the broad class of fluctuations observed in the ionospheric plasma as *traveling ionospheric disturbances (TIDs)*. In the framework of the current study, these TIDs are related to the ionospheric plasma fluctuations, which result from neutral-ion/electron coupling driven directly by AGW fluid motions.

The Hunga Tonga-Hunga Ha'apai volcano's series of eruption events on the 15 January 2022, have found interest from a broad range of scientific communities, from solid Earth and ocean dynamics (Carvajal et al., 2022; Kubota et al., 2022; Poli & Shapiro, 2022), to ground-based infrasound (Chunchuzov et al., 2023; Matoza et al., 2022), and to aeronomy and space physics (e.g., Wright et al., 2022; Themens et al., 2022; S.-R. Zhang et al., 2022). This event provided a unique opportunity to advance our understanding of NH-induced waves from a large-magnitude source. Estimated as a megatons-equivalent event (Matoza et al., 2022; Vergoz et al., 2022), the eruptions generated a very broad spectrum of waves that propagated globally over several days (S.-R. Zhang et al., 2022). The reports suggest complex and nonlinear AGW dynamics in the atmosphere, impacting the state of the stratosphere (Khaykin et al., 2022; Millan et al., 2022) and ionosphere (Astafyeva et al., 2022; Harding et al., 2022;

He et al., 2023; Li et al., 2023; Vadas et al., 2023a), generating effects locally and in the magnetically-conjugate ionosphere via coupling through the plasmasphere (Aa et al., 2022a; Harding et al., 2022; Lin et al., 2022). Nevertheless, there is still a lack of understanding of the generation and evolutions of various wave modes and, especially, of their observable effects on the upper layers of the atmosphere and ionosphere.

This study is devoted to a comprehensive investigation of the characteristics and morphology of atmospheric and ionospheric fluctuations arriving along with Lamb wave modes over the continental part of the United States (CONUS). There, signals were detected with unprecedented spatial and temporal resolution at key altitudes ranging from surface to the thermosphere. We show that the atmosphere and ionosphere exhibited propagating AGWs and TIDs over CONUS, that accompany the predicted arrivals of Lamb wave modes in time. Along with the variability of characteristics of fluctuations, we demonstrate the consistency in their amplitude modulations in time, projected over height, revealing the correlations between the AGW fields propagating near the surface and those extending to hundred(s) of km above the Earth's surface. From joint multi-layer/-instrument data analyses, we also find consistency in the times of arrival of several packets of AGWs and TIDs to CONUS to the set of Hunga volcano eruption events over 8 hr. In addition, with a set of Lamb wave mode ray-tracing results, we demonstrate the role of the ambient meteorology at the time of wave propagation, to assess how the incorporation of atmospheric state parameters and winds based on data assimilation (DA) and reanalysis can more effectively describe the evolution of the observed waves than empirical/climatological models. The results suggest future opportunities to use the atmosphere not only as a sensor for the detection of NH-generated waves, but toward using the information carried by AGW/TID signals to quantitatively constrain the dynamics of NH processes. At the same time, we demonstrate the complexity of vertically-evolving AGWs, which may include effects of the inhomogeneity of the atmosphere and topography, as well as revealing anisotropies of AGW sources.

In Section 2 we discuss the instrumentation, its configuration, measurements and their processing, as well as our ray-tracing methodology for modeling Lamb wave modes. Section 3 presents the observations, modeling and their analysis; Sections 4 and 5 include the discussion and summary of the major scientific findings of our investigation, as well as future studies that we are undertaking.

2. Instrumentation, Data Sets and Modeling Methodology

In this section, we discuss the observations and modeling used in this study; additional details are provided in Supporting Information S1. Figure 1a illustrates the locations of surface barometer sites, Global Navigation Satellite System (GNSS) signal receivers and a Fabry-Perot Interferometer (FPI) site. Red and green circles define map-projected fields of view of red (630.0 nm) and green (557.7 nm) line airglow observations, with a rhombus representing the location of imagers at Capitol Reef Field Station, Utah. Figure 1b illustrates the locations of low frequency (LF) radio receivers and the Fallon, NV, LORAN-C transmitter, as well as reflection points and Frensel zones at 80 km altitude (their exact coordinates are provided in Supporting Information S3). As the LORAN-C experiment was part of a unique campaign and these data were obtained fortuitously, we provide the schematic representation of the geometry of observations in Figure 1c.

First, to provide a temporal reference for the arrival and morphology of AGWs and their propagation over CONUS, we demonstrate the National Oceanic and Atmospheric Administration (NOAA) GOES-16/17 satellites' Advanced Baseline Imager Level 1b (L1b) Full Disk and Mesoscale Radiance observations in Section 3.1. The spatial resolution of the instrument in Full Disk mode of observations is 2 km at nadir and the coverage is of 83° local zenith angle. Full disk maps are spatially smoothed using a two-dimensional (2D) moving average filter. Then, to extract fluctuations, we apply the fourth time derivative with fourth order accuracy using a central difference scheme to each pixel of full disk map image. While full disk maps provide us with the opportunity to investigate fluctuations propagating obliquely through the atmosphere from the volcanic source to and over CONUS, the 10-min cadence of successive images lacks the necessary temporal resolution to achieve the investigation of short-period fluctuations (Horvath et al., 2023). To address the characteristics of fluctuations over CONUS, we additionally use 1-min GOES mesoscale scan imagery that covers regions southwest of CONUS. For this data set, we calculated brightness-weighted temperature based on Channel 11 radiance observations, spatially smoothed them using a 2D moving average filter and then calculated second order time derivative of a second order accuracy using a central difference scheme for each pixel of image. We note that such difference methods may not have a uniform sensitivity for all periods/wavelengths, although they are sufficiently effective to track the propagation of the primary fluctuations discussed below. The details of data processing are provided in Text S1.2 in Supporting Information S1.

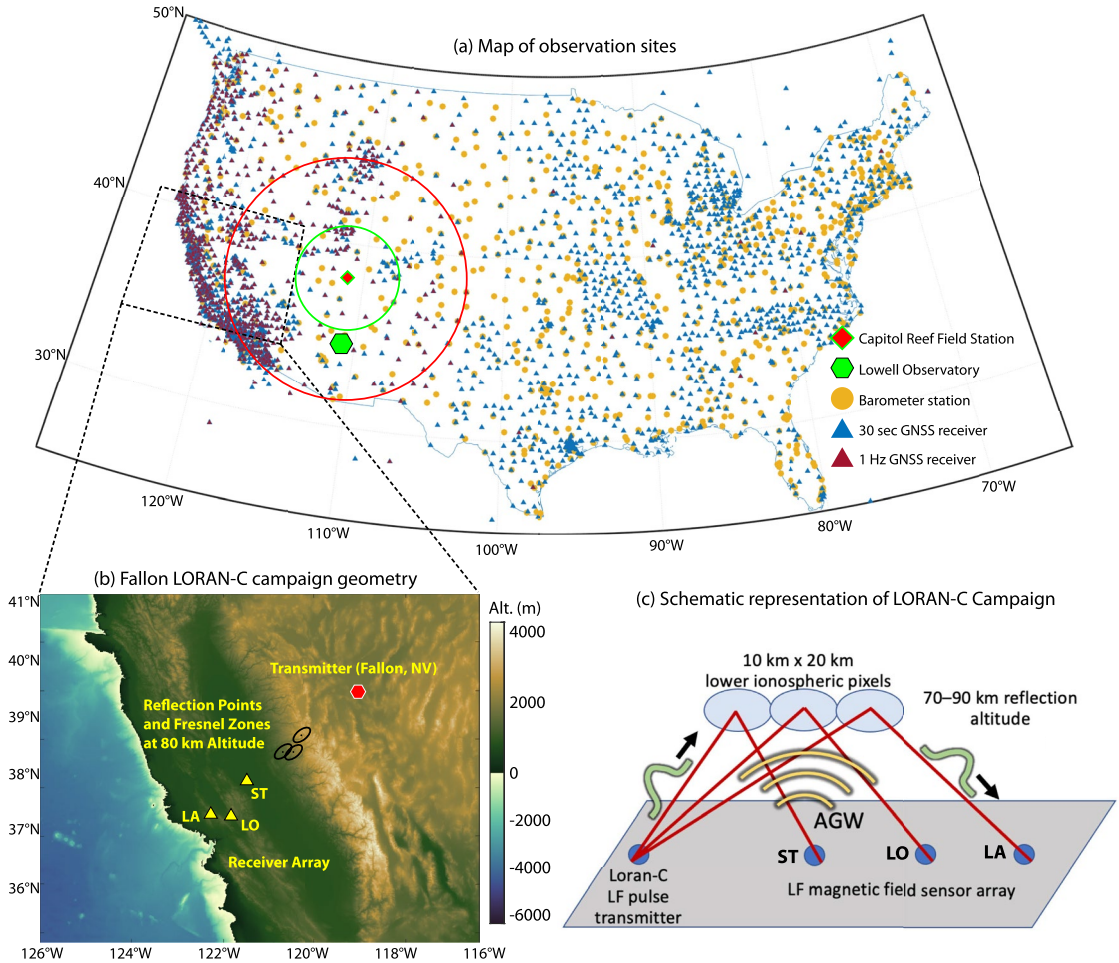

Figure 1. (a) Map of Automated Surface Observing Systems network barometer stations, 1, 15, and 30 s sampling rate Global Navigation Satellite System receivers, and locations of Fabry-Perot Interferometer and airglow imagers used in this study. (b) The locations of the transmitter, receivers, respective reflection points and Frensel zones at 80 km altitude of the Fallon LORAN-C campaign. (c) Schematic representation of the geometry of Fallon LORAN-C campaign observations (the locations of receivers and transmitter are not in scale and the picture serves only for illustrative purposes).

We further analyze observations from 844 barometers of 1 min sampling rates in Section 3.2. These belong to Automated Surface Observing Systems (ASOS) network, which is a joint effort of the National Weather Service, the Federal Aviation Administration, and the Department of Defense (DoD) (Nadolski, 1998). To extract fluctuations from barometer observations, we applied various filters that will be highlighted in the discussion of the results. The details of this data set are provided in Text S1.1 in Supporting Information S1. The modeling results of Lamb wave mode ray-tracing are also overlaid onto the GOES-16/17 satellite and surface pressure observation images, as will be discussed in related sections.

Next, we present observations of green (557.7 nm) and red (630.0 nm) line airglow emissions in Section 3.3. The source of the green line emission is the O^1S species, which is assumed to arise with peak density at ~95 km altitude. The red line results from the dissociative recombination of O_2^+ leading to O^1D, and originates from 200 to 300 km altitudes. Since it was nearly a full-moon night, moonlight contaminated data from most airglow imagers, except Midlatitude Allsky-imaging Network for GeoSpace Observations (MANGO) imagers installed at Capitol Reef Field Station, Utah (38.18°N/111.18°W), which is surrounded by mountains (Bhatt et al., 2023). The spatial coverage by green and red line imagers are ~500 and ~1,800 km in diameter respectively, and the integration times are 2 and 4 min, respectively. The imagers are sensitive to horizontal scales (wavelengths) of ~2–250 km (green) and ~7–900 km (red). The images presented are created with sequential differencing of the observations (essentially providing a high-pass filter), with mean values removed from each image. The integration time sets the Nyquist sampling limit of observable wave periods at 4 min (green) and 8 min (red). Other details of data processing are provided in Text S1.3 in Supporting Information S1.

The FPI is optimized to perform thermospheric red line airglow observations of the 630.0 nm emission. The data used in this study are from the MANGO Network instrument operated at the Lowell Observatory site (34.752°N/111.423°W). The temporal averaging (integration) of the image samples during the wave event was ∼2.5 min, taken at a cadence of ∼8 min, and no further filtering is applied. Thus, the FPI is sensitive to all wave periods >5 min, but periods <16 min are expected to be aliased. The algorithms to estimate winds, as well as data analysis and quality control methodologies are discussed in detail by Makela et al. (2012); Harding et al. (2014, 2019, 2021), as well as in Text S1.4 in Supporting Information S1.

Following Section 3.4 demonstrates the results of our campaign of signal measurements in the ionospheric D-region. The LF-band LORAN-C transmitter at Fallon, Nevada, was operated in a campaign mode, with receivers distributed throughout the San Francisco Bay Area at Stockton (ST), Los Altos (LA), and Lick Observatory (LO) (see schematic illustration of the experiment in Figure 1c). The LORAN transmitter radiates a 90–110 kHz pulse with GPS-synchronized timing that is reflected from the ionospheric D or E layers at 70–90 km altitude. Receiving this pulse enables continuous measurements of the vertical motion of the D region electron density (Fox, 2006; Iwata & Ishikawa, 1974), thus detecting mechanical fluctuations there from external sources. As collected with 2 s sampling rate continuously on 15 January, we expect that these observations cover a sufficiently broad range of periods of fluctuations in the D region of the ionosphere, including those driven by AGWs having periods from minutes to hours. We note that the averaging of observations occurs over the ∼20 km long Fresnel zone patch, thus filtering horizontally-propagating acoustic wave fluctuations of tens of seconds. Other details of the processing methodology are given in Text S1.5 in Supporting Information S1.

Finally, Section 3.5 presents our analysis of TID signals in GNSS total electron content (TEC) observations. TEC represents an estimate of the integrated value of electron density between the ground-based receiver and the transmitter (here installed on medium Earth orbit satellites). It is derived from the observations of GNSS signal group delays and phase advances resulting from dispersion in the ionosphere, and widely used to investigate the state of ionospheric plasma and its fluctuations driven by AGWs (Komjathy et al., 2016; Mannucci et al., 1998; Parkinson et al., 1995). The processing of GNSS data and derivation of TEC from these data were performed using software developed at Embry-Riddle Aeronautical University. The locations of TEC observations are linked to the piercing of the ionospheric shell at 300 km height by lines-of-sights between ground-based receivers and satellites. The ionospheric shell corresponds to the approximate altitude of maximum electron density in the ionosphere, the region of predominant GNSS signal delays and thus observable fluctuations. GNSS TEC observations are applicable for the analysis of fluctuations of up to ∼2 hr periods, as the ground receivers tracks GNSS satellite for up to several hours, depending on the geometry of observations. The spatial resolution of maps of GNSS TEC 15/30 s sampling rate observations over CONUS used in this study is on average ∼0.1–0.2° in latitude and longitude, depending on the region and time, covering TIDs driven by AGWs from minutes of periods. Additional data processing methodology details are provided in Text S1.6 in Supporting Information S1.

2.1. Ray-Tracing of Lamb Wave Modes

The Lamb wave mode propagation is investigated via ray-tracing. The Earth's atmosphere is assumed everywhere to be nearly isothermal so that vertically-averaged quantities describing Lamb wave propagation can be defined (see details in Bretherton (1969)). The disturbance due to the Lamb wave mode is considered localized near a surface. The wavefront, which is supposed to be orthogonal to the ground, propagates horizontally along the Earth's surface that is modeled as an ellipsoid via the World Geodetic System 1984 (WGS 84). This wavefront is therefore described by horizontal rays that emanate from the eruption location. Let θ be a parameter representing the emission angle of a ray with respect to a reference axis centered at the eruption site and $\boldsymbol{x}_H(t,\theta)$ be the position on the Earth's surface of that ray at time t. Let $\bar{c}(\boldsymbol{x}_H,z)$, $\bar{\boldsymbol{v}}(\boldsymbol{x}_H,z)$, $\bar{p}(\boldsymbol{x}_H,z)$ and $\bar{\rho}(\boldsymbol{x}_H,z)$ be the local vertical profiles of the atmospheric speed of sound, horizontal wind vector, pressure, and density, respectively, with z the altitude. Define the vertically-averaged values $c_L(\boldsymbol{x}_H)$ and $\boldsymbol{v}_L(\boldsymbol{x}_H)$ as (Pierce & Posey, 1971)

$$\frac{1}{c_L^2}=\left\langle\frac{1}{\bar{c}^2}\right\rangle,\quad \boldsymbol{v}_L=\langle\boldsymbol{v}\rangle, \tag{1}$$

where, for any altitude-dependent function $f(z)$ (Bretherton, 1969; Pierce & Posey, 1971),

$$\langle f(z)\rangle = \frac{\int_0^\infty \mathcal{E}(\boldsymbol{x}_H, z) f(z) dz}{\int_0^\infty \mathcal{E}(\boldsymbol{x}_H, z) dz}, \quad \mathcal{E}(\boldsymbol{x}_H, z) = \frac{\bar{p}^{2/\gamma}(\boldsymbol{x}_H, z)}{\bar{\rho}(\boldsymbol{x}_H, z)}. \tag{2}$$

Then, for each θ, the trajectory of the corresponding ray $\boldsymbol{x}_H(t, \theta)$ is governed by the ordinary differential equations (Pierce & Posey, 1971)

$$\begin{aligned} \frac{d\boldsymbol{x}_H}{dt} &= \boldsymbol{c}_g, \\ \frac{d\boldsymbol{k}_H}{dt} &= \left[\nabla \boldsymbol{c}_g\right] \cdot \boldsymbol{k}_H, \end{aligned} \tag{3}$$

where $\boldsymbol{k}_H$ is the horizontal wavenumber vector and $\boldsymbol{c}_g = (c_L \boldsymbol{k}_H / \|\boldsymbol{k}_H\| + \boldsymbol{v}_L)$ is the group velocity for Lamb wave modes. System (3) requires the specification of the ambient atmospheric flow for the calculation of c_L and $\boldsymbol{v}_L$ at each instant of time t and ray position $\boldsymbol{x}_H(t, \theta)$. It is solved numerically via the forward Euler method.

This study focuses on the propagation of Lamb wave modes toward and over CONUS. To investigate the impacts of background atmospheric state and wind specifications on Lamb wave mode propagation, four simulations are carried out. In Simulation #1, the atmospheric pressure, density, and speed of sound fields are defined via the global empirical model NRLMSISE-00 (Picone et al., 2002), while the winds are provided by the global empirical model HWM-14 (Drob et al., 2015). In Simulation #2, the winds are set to zero, which allows evaluating their effects on Lamb wave mode rays. The background atmospheric state and winds in Simulation #3 are derived via DA reanalysis experiments using the Navy Global Environmental Model (NAVGEM). Details of these DA experiments and the derivation of final reanalysis products for these ray-tracing experiments are provided in Text S2 in Supporting Information S1. Briefly, products are issued as global meteorological reanalysis fields from 0 to 500 km altitude at a 1-hr time cadence spanning 14–15 January 2022. Since the DA operated on a standard 6-hr update cycle, hourly fields between the standard analysis times of 0, 6, 12, and 18 UT were based on 1–5 hr forecasts using the latest analysis state as atmospheric initial conditions for the forecast (Eckermann, 2023; Eckermann et al., 2023; Emmert et al., 2021; Hunt et al., 2007; Koch & Saleeby, 2001; Koshin et al., 2020; Laskar et al., 2021). This 1-hr reanalysis cadence yields superior temporal definition of solar and lunar tides relative to 6-hr reanalysis (see, e.g., Figure 12 and associated discussion in Eckermann et al. (2018)). Atmospheric densities, temperatures, pressures, specific heats and horizontal wind vectors from these reanalysis products were then continuously interpolated in space and time to each ray's current space-time location along its evolving group trajectory and used to compute relevant vertically-averaged values c_L and $\boldsymbol{v}_L$ at each instant of time t and ray position $\boldsymbol{x}_H(t, \theta)$. Finally, in Simulation #4, the background atmospheric state is again specified via the NAVGEM reanalysis but without the inclusion of winds.

3. Results

Based on the International Seismological Centre (ISC) catalog and observations, the main sequence of events occurred between 04:07 and 04:40 UT on 15 January 2022. The strongest event of estimated magnitude 5.3 mb (short-period body wave-type magnitude) occurred at 04:14:54 UT, 20.55°S/175.39°W (see Table in Figure 11b). We mark this sequence as Event #1, as it is interpreted to have generated the packet of Lamb wave modes first reaching CONUS (as discussed in Section 3.6). Next, for simplicity, we relate the events that occurred between 05:03 and 06:06 UT from Figure 11b as Event #2 that produced a second clearly discernible packet of Lamb wave modes. Overall, there was a sequence of events between 3 and 12 UT, although of substantially smaller magnitudes than in the above mentioned windows. Thus, in subsections below we focus on the observations related to Events #1 and #2, as they produced the strongest signals over CONUS. The signatures of AGWs and TIDs potentially related to later events are discussed in Section 3.6.

3.1. Global Tropospheric Observations

We start with NOAA geostationary GOES-16 and GOES-17 satellite 10-min tropospheric observations that provide a synoptic perspective on AGW propagation from the volcano to and over CONUS. Except panel (c), Figure 2 presents a set of 10.3 μm nadir radiance Full Disk images observed from both satellites, postprocessed

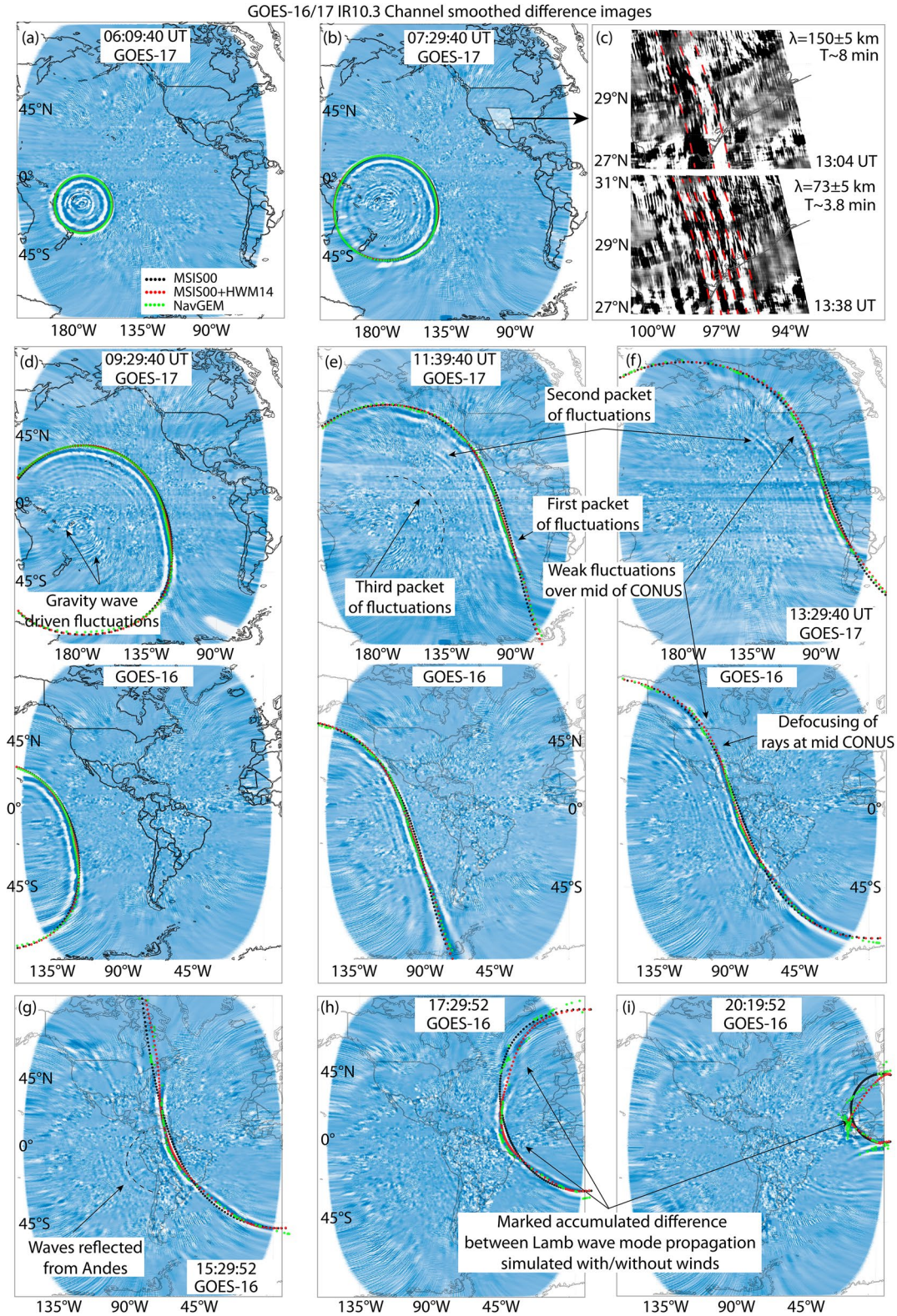

Figure 2. Snapshots of GOES-16/17 IR10.3 infrared observations and simulated Lamb wave ray-tracing results (red, black, and green dots, as discussed in the text). The panels with blue-white colormap represent the processed images of 10-min Full Disk observations. Panel (c) with black-white colormap illustrates the results of 1 min GOES-16 mesoscale observations over west part of Continental United States.

to isolate perturbations as discussed in Section 2. The panels are complemented by Lamb wave mode ray-tracing modeling results. Red, black and green dots represent ray positions at the time of GOES-16/17 image snapshots from simulations #1, #2, and #3, respectively, as introduced in Section 2.1. As discussed above, according to the ISC catalog, the strongest Event #1 occurred at 04:14:54 UT. At the same time, previous analyses of near- and far-field surface pressure fluctuations and their back-projections pointed to ∼04:28 UT as the time of strongest pulses observed (Wright et al., 2022; Yuen et al., 2022). Indeed, with a set of simulations, we found the best agreement between GOES-16/17 observations and Lamb wave mode ray-tracing using an initial time of 04:28 UT and so this time was used in all simulations presented here. For reference, we provide the animations from simulations with an initial time of 04:14:54 UT in Movies S2 and S4.

Strong perturbations (in comparison with the background and those driven by tropospheric activity) appeared minutes after the Event #1 (see animation in Movies S1–S4). The fluctuations were concentric and propagated away from an eipcenter at the volcano's location (Figures 2a, 2b, and 2d). The arrival of tropospheric fluctuations at CONUS occurred at ∼11:40 UT (Figure 2e). We note their markedly smaller amplitudes over the mid-latitude part of CONUS, while the fluctuations to the south of CONUS, as well as its northern regions and Canada, are of comparatively high amplitudes (Figure 2f). While AGWs reach the Atlantic Ocean, their observable fluctuations were still of comparatively lower amplitudes to the north of CONUS relative to the south (Figures 2g and 2h). Such variability can be discerned based on observations with both GOES-16 and GOES-17 satellites and plausibly relates to wave propagation dynamics rather than observational nuances.

One can also discern two sets of fluctuations of smaller amplitudes, propagating from the position of the volcano after the Event #1 with similar apparent horizontal speed of phase fronts (hereafter, v_ϕ) shown in Figures 2e and 2f. We propose that these fluctuations were driven by AGWs excited by the following events, as discussed in Section 3.6. Some fluctuations propagated comparatively slowly from the position of the volcano with estimated v_ϕ of 57–178 m s^{-1} and can be associated with gravity waves (Figure 2d). Finally, it is interesting to highlight fluctuations propagating back to the Pacific Ocean after reaching Andes (Figure 2g), apparently due to reflection, as identified also by Wright et al. (2022). These reflected waves propagated over CONUS at ∼18–20 UT (see the animation in Movies S3 and S5).

For the first hours after Event #1, the Lamb wave mode ray-tracing results from all simulations closely match the observations (Figures 2a–2d). However, over CONUS, Simulation #1 produces faster speeds of rays over mid-latitude and north of CONUS than found in the observations (Figure 2f). The spatial difference between ray arrivals from Simulations #1 and #2 constitutes ∼1° in the mid-latitude part of CONUS and up to 3° over Canada (∼5–16 min difference in arrival times, respectively). Further to the Atlantic ocean and in the proximity of the antipode over Africa, the differences between Simulations #1 and #2 are even larger, constituting ∼5–8° and pointing to the importance of wind effects on Lamb wave mode propagation. Here, GOES-16 observations, being at the edge of instrument field-of-views, cannot be clearly analyzed, although Wright et al. (2022) demonstrated Lamb wave modes-driven fluctuations in Meteosat SEVIRI observations further to the east over the Atlantic Ocean and beyond.

Simulation #3 results, incorporating NAVGEM meteorological fields, provide the best agreement with GOES-16/17 observations, including Lamb wave mode propagation over CONUS. While being fairly similar to Simulations #1 and #2 prior to ray arrivals over CONUS (Figures 2a–2d), the results of Simulation #3 differ markedly over CONUS. Rays to the south of CONUS propagate faster than rays over mid- and north-latitudes of CONUS (Figures 2f–2h). Moreover, although the rays in Simulations #1 and #2 preserve their comparatively constant density over the whole range of distances, Simulation #3 indicates marked deflection of rays and their focusing to the south and north of CONUS (Figures 2f–2h). The lateral defocusing of rays over mid-latitudes of CONUS is consistent with weak signals for GOES-16/17 satellite observations discussed above. The results between simulations differ to a marked extent as rays reach Africa (Figure 2i). Simulations #1 and #3 replicate phase fronts in the proximity to the antipode position much better than Simulation #2.

We estimate the average v_ϕ to be in the range of 300–330 m s^{-1}, consistent with expected speeds of Lamb wave modes (cf. Section 1). To better investigate the wavelength and periods of fluctuations, we used GOES 1-min observations over isolated region over CONUS, as shown in Figure 2c. These observations suggest the propagation of comparatively large scale fluctuations of wavelength $\lambda_\phi = 150 \pm 5$ km. Followed by them is a train of

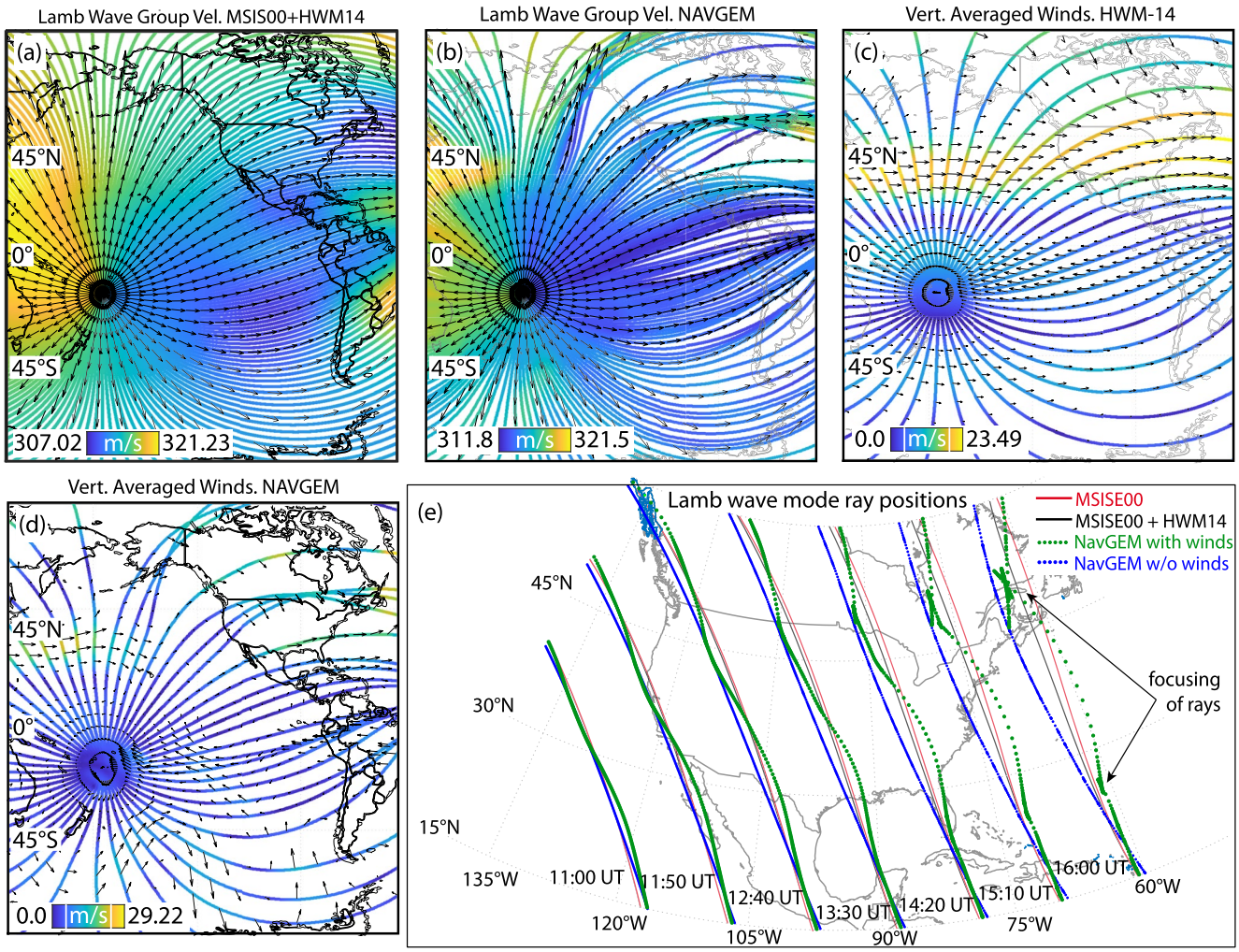

Figure 3. Lamb wave mode group velocities and vertically averaged winds from (a, c) Simulation #1 (NRL-MSISE00/HWM14) and (b, d) Simulation #3 (data assimilation reanalysis experiments using the Navy Global Environmental Model). (e) Snapshots of Lamb wave mode ray positions at seven instances of time over Continental United States from Simulations #1–4.

smaller-scale fluctuations of $\lambda_\phi = 73 \pm 5$ km. Based on the estimate of their phase speeds of 300–330 m s^{-1}, the ground-based period of these fluctuations lies in the range of 3–8 min.

Next, to illustrate the role of the atmospheric state and winds, Figures 3a–3d show calculated absolute group velocities and vectors of simulated Lamb wave mode rays, and absolute values and group propagation vectors of vertically averaged winds calculated for each ray over the region of GOES-17 satellite observations. Panels a and c, and b and d illustrate the results of the same simulations, but with different numbers of rays to make illustrations more easily readable. Both Simulations #1 and #3 demonstrate comparable ranges of Lamb wave mode group speeds of ~307–321 m s^{-1} with a sharp gradient of speeds in zonal direction (Figures 3a and 3b). However, clear differences arise in ray propagation directions between simulations. Simulation #3 exhibits marked lateral deflection of rays before reaching CONUS. This effect is most apparent over CONUS, with focusing of rays to the south and north and notably smaller density of rays in mid-latitudes over CONUS. At the same time, Simulation #1 exhibited consistent density of rays over the whole CONUS.

The results demonstrate the importance of winds in Lamb wave mode propagation, especially to far-fields (Figures 3c and 3d). HWM-14 model-based results suggest dominant westward vertically averaged winds at ±15° from equator (~0.3–1 m s^{-1} absolute values) and eastward vertically averaged winds in the range of ~40–55°N that reach absolute values ~23 m s^{-1}. This explains earlier arrival of simulated Lamb wave mode rays over mid-latitudes of CONUS (Figures 2g–2i), relative to later arrival times over the equator in Simulation #1 in

comparison with Simulation #2, respectively (Figures 2f and 2g). At the same time, Simulation #3 also suggests the presence of strong meridional component of vertically averaged winds, which impact rays in 25°S–25°N range of latitudes, as well as rays propagating to the north and northeast from the volcano, overall reaching ∼29 m s^{-1}. The cumulative wind effects eventually result in a notable deflection of rays as they reach CONUS.

Finally, we provide the snapshots of ray positions at seven separate times over CONUS in Figure 3e, where, additionally, we include Lamb wave mode ray-tracing simulation results using NAVGEM reanalysis, but excluding its winds (Simulation #4). As mentioned above, although the arrival of rays to the west coast of CONUS is fairly similar between all 4 simulations, we find a dramatic difference between simulations #1 and #2, as well as #3 and #4 over CONUS. We highlight that winds in Simulation #3 played a decisive role in lateral deflection of rays over CONUS. In comparison with Simulation #4 (NAVGEM without winds), Simulation #3 includes earlier arrivals of rays to the south of CONUS and later to the north, with much less dense rays at mid-latitudes of CONUS. Finally, Simulation #3 exhibits focusing of rays over Canada and to the south of CONUS, which becomes particularly apparent to the west of Florida and further to the Atlantic Ocean.

3.2. CONUS Surface Observations

Here, we discuss ground-level pressure observations from the ASOS network over CONUS (see the animation in Movie S7). Time-distance diagrams of 180 min high-pass filtered observations reveal two dominant packets of fluctuations with a time gap of ∼2 hr between (Figure 4a). The first packet reached CONUS at ∼11:40 UT, consistent with fluctuations in GOES-16/17 satellite observations. Although propagating as a compact set of fluctuations closer to the west coast (Figure 4h), two separate phase fronts can be discerned farther to the east, propagating with the estimated horizontal speeds (v_ϕ) of 307 and 345 m s^{-1} (Figures 4a and 4i). The separation between the two fronts can be seen at mid-latitudes of CONUS (Figure 4i), with faster fluctuations propagating to the south and slower to the north. Both phase fronts can be discerned in pressure signals, as shown for the station GSO (Piedmont Triad International Airport, North Carolina) located at 36.1°N/79.94°W (Figure 4g), whereas from stations to the south, for example, GIF (Winter Haven Airport, Florida), we find a single pressure pulse of markedly stronger amplitude (Figure 4d). Along with a dominant period of ∼20–50 min, short period perturbations of ∼3 min propagated within the packet of fluctuations (e.g., station APC shown in Figure 4f), also discernible from time-distance diagram of 10 min high-pass filtered pressure observations (Figure 4c). They also exhibited fast and slow v_ϕ, in the same manner as discussed above. In comparison, the observations over Alaska do not reveal any variability in speeds or amplitudes of phase fronts from the leading packet of Lamb wave modes, which propagated consistently with v_ϕ of ∼310–317 m s^{-1} (Figure 4b).

The second packet of weaker fluctuations, reaching CONUS at ∼13:30 UT (i.e., ∼1.7–2 hr later than the first packet), propagated with v_ϕ comparable to the first packet of ∼301–307 m s^{-1} through the whole range of distances (Figures 4a and 4j). The periods of dominant fluctuations lie in the range of 14–25 min, although short period fluctuations of minute periods are present too. The second packet did not include any notable variability of speeds and propagated consistently over CONUS (Figure 4a). Later arriving fluctuations had similar v_ϕ, but very small amplitudes, and are discussed separately in Section 3.6.

We highlight a marked variability of pressure fluctuation amplitudes (Figure 4k). Whereas peak values of ∼160 Pa occur to the south and northwest of CONUS (e.g., stations GIF, BOI, and APC as illustrated in Figures 4d–4f), the regions from the southwest to northeast of CONUS included fluctuations of notably smaller amplitudes of 20–60 Pa (e.g., station GSO, Figure 4g). The perturbations generated by the second packet are in the range of ∼15–30 Pa over CONUS, and only ∼5 Pa over Alaska. Nothing decisive can be said about the patterns of fluctuation periods; whereas in the region between depicted dashed lines (Figure 4l) the fluctuations had dominant periods of 40–50 min and periods of ∼30 min to the north of that region, there is a subset of stations that represent comparable periods of dominant fluctuations over the whole CONUS.

The Lamb wave mode ray-tracing Simulations #1 and #2 agree well to the west of CONUS in times of Lamb wave mode arrivals revealed from pressure fluctuation observations (Figure 4h), whereas farther to the east these ray-tracing results differ modestly (Figure 4i). In particular, to the south and mid-latitudes of CONUS, they lag by ∼2° (i.e., ∼12 min), and to the north Simulation #1 rays advance by ∼5° (i.e., ∼30 min). Simulation #3 rays replicate both the lag of fluctuations to the north and their advance at mid- and south-latitudes of CONUS to much better extent. Moreover, Simulation #3 explains the comparatively weak pressure fluctuations illustrated in Figure 4k, as ray densities over the mid-latitude region are markedly lower due to their deflection to the north and south of

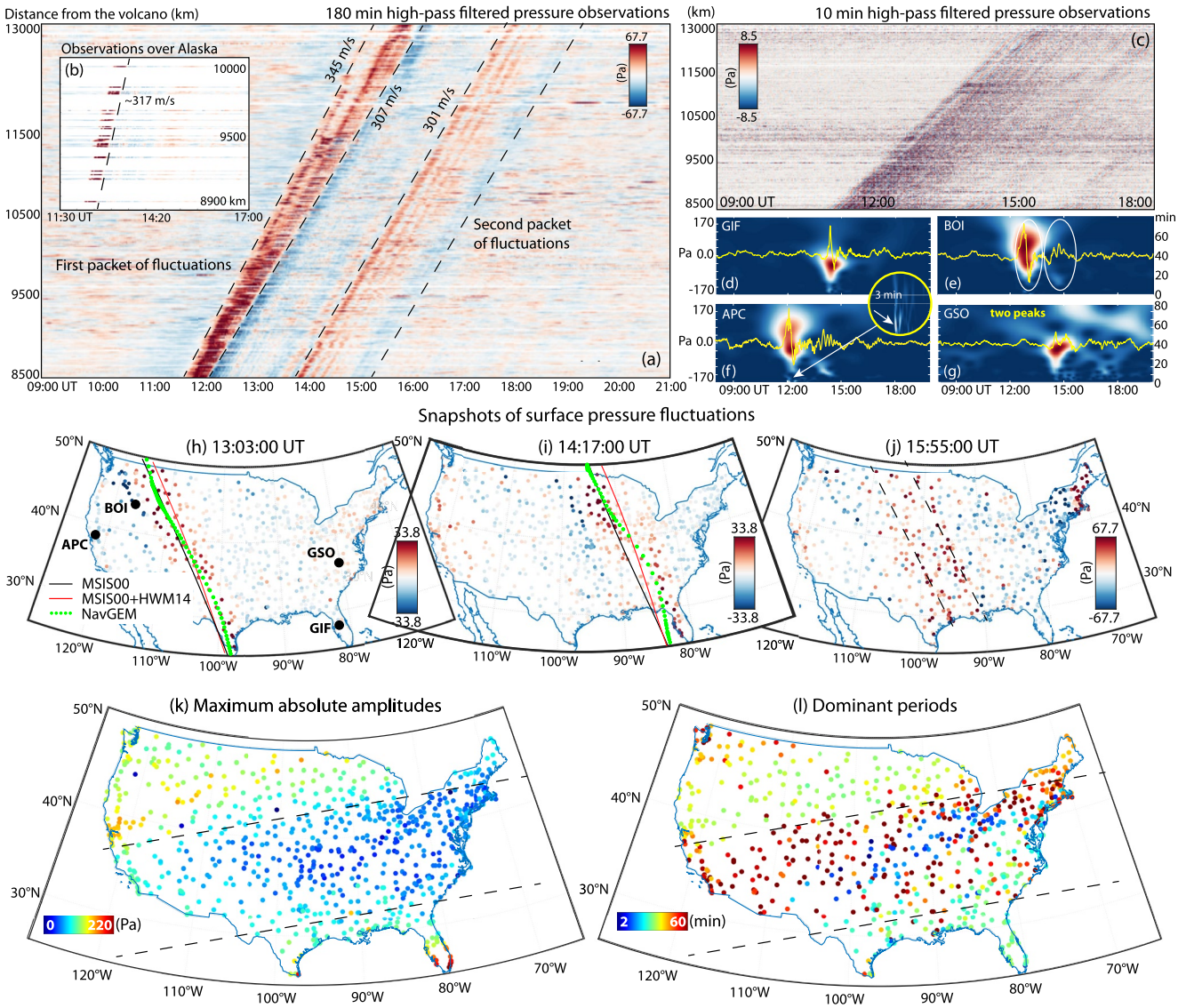

Figure 4. Time-distance diagram of filtered surface pressure observations from Automated Surface Observing Systems network stations over (a) Continental United States and (b) Alaska. (c–f) Time-series of the same filtered pressure observations for stations APC, BOI, GSO, and GIF with their Morlet wavelet transforms. (g–i) Snapshots of filtered pressure observations overlaid onto geographic map at three time epochs. Amplitudes of fluctuations are defined as colors of circles. Solid red and black lines define Lamb wave front simulated in ray-tracing simulation with and without winds, respectively. (j) Time-distance diagram of 10 min high-pass filtered surface pressure observations. (k) Maximum reached absolute amplitudes (k) and (l) dominant periods from 180 high-pass filtered observations.

CONUS. However, Simulation #3 rays still exhibit ~10 min lags to the south and advance to the north. Finally, none of the simulations include wavefronts of ~345 m s^{-1}, as found in pressure observations (Figures 4a and 4c).

3.3. Airglow Imagers and Fabry-Perot Interferometer Observations

Figures 5 and 6 illustrate the snapshots of processed green and red line airglow imager observations, respectively, from the MANGO imager sites at Capitol Reef Field Station in Utah. The northwest part of the imager's field of view was contaminated with moonlight and blocked by trees or buildings; these parts of the images are masked for visualization purposes. Animations of the imaging data are provided in Movie S1.

The first fluctuations in the green line images appeared to the southwest at ~12:04 UT (Figure 5a). The leading ones had smaller estimated horizontal wavelengths (λ_x) of 29–60 km and smaller amplitudes (Figures 5b–5d). Later fluctuations were of larger λ_x of 80–100 km and of larger amplitudes (Figures 5g–5p). We estimate the v_ϕ of these

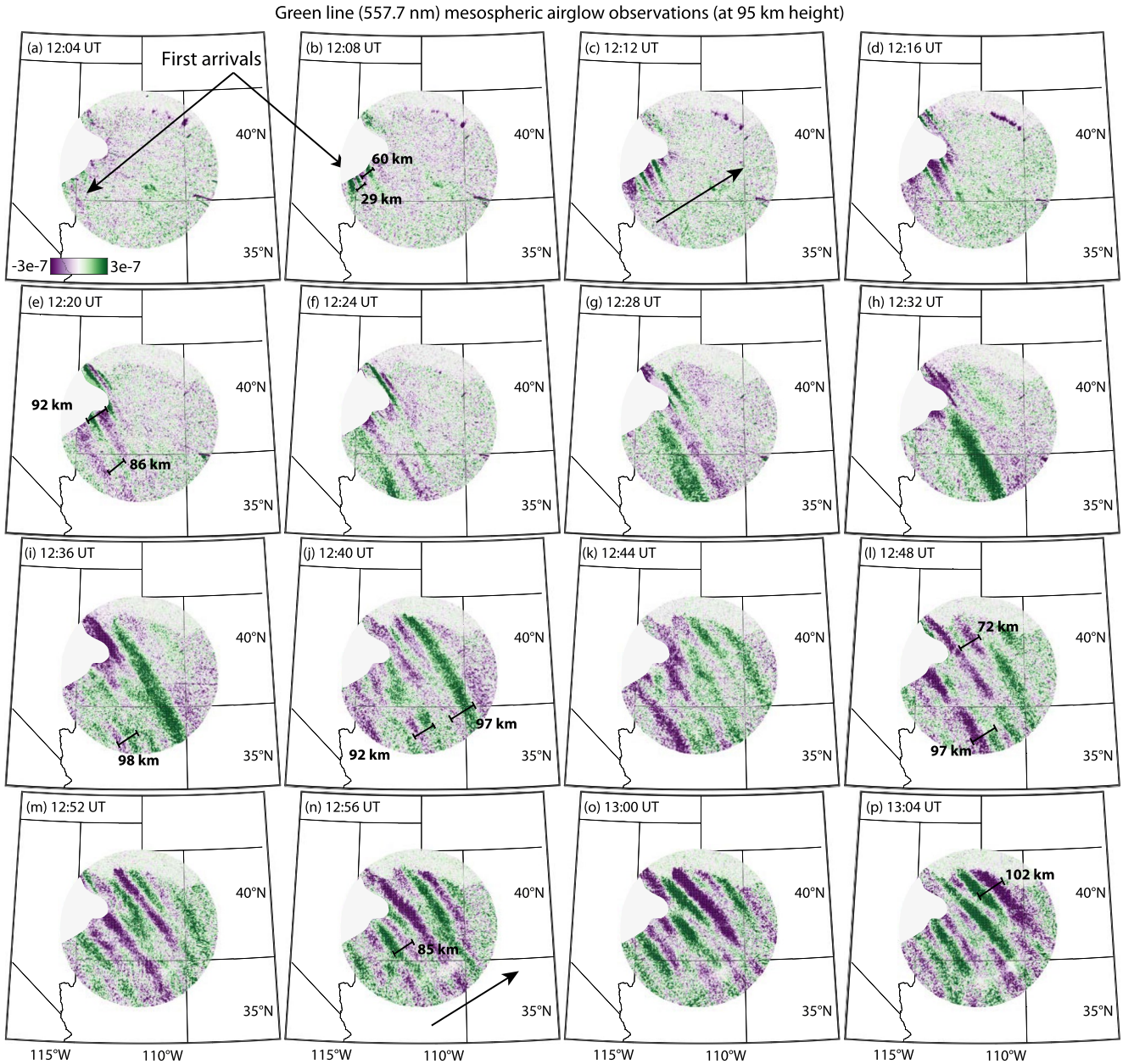

Figure 5. Mesospheric 557.7 nm green line emission observations. The difference images for 16 time epochs are unwarped onto the Continental United States map. The animation is provided in Movie S1.

fluctuations to be in the range of 295–330 m s^{-1}. The arrival of these fluctuations is consistent with the arrival of Lamb wave modes to the west coast of CONUS discussed earlier based on surface pressure, GOES-16/17 nadir imagery and ray-tracing simulation results. Their propagation is predominantly to the northeast-east through to the end of observations at 13 UT, when contamination by sunlight prohibits further investigation of observations (~6 a.m. local time).

Similar to the green line, the first fluctuations in the red line images appeared to the southwest at ~12:00 UT (Figures 6a–6d). The whole packet of fluctuations also propagated predominantly to the northeast. We estimate λ_x of fluctuations in the range of 150–226 km and v_ϕ of 320–335 m s^{-1} (Figures 6l–6p). Such a wide range of estimated λ_x and v_ϕ results from AGWs that were potentially superposed and thus represent a complex configuration (particularly at later times). The comparatively lower sampling rate of 4 min also contributes to this broader range. The fluctuations can be seen through to the end of observations at 13:00 UT (Figures 6l–6p).

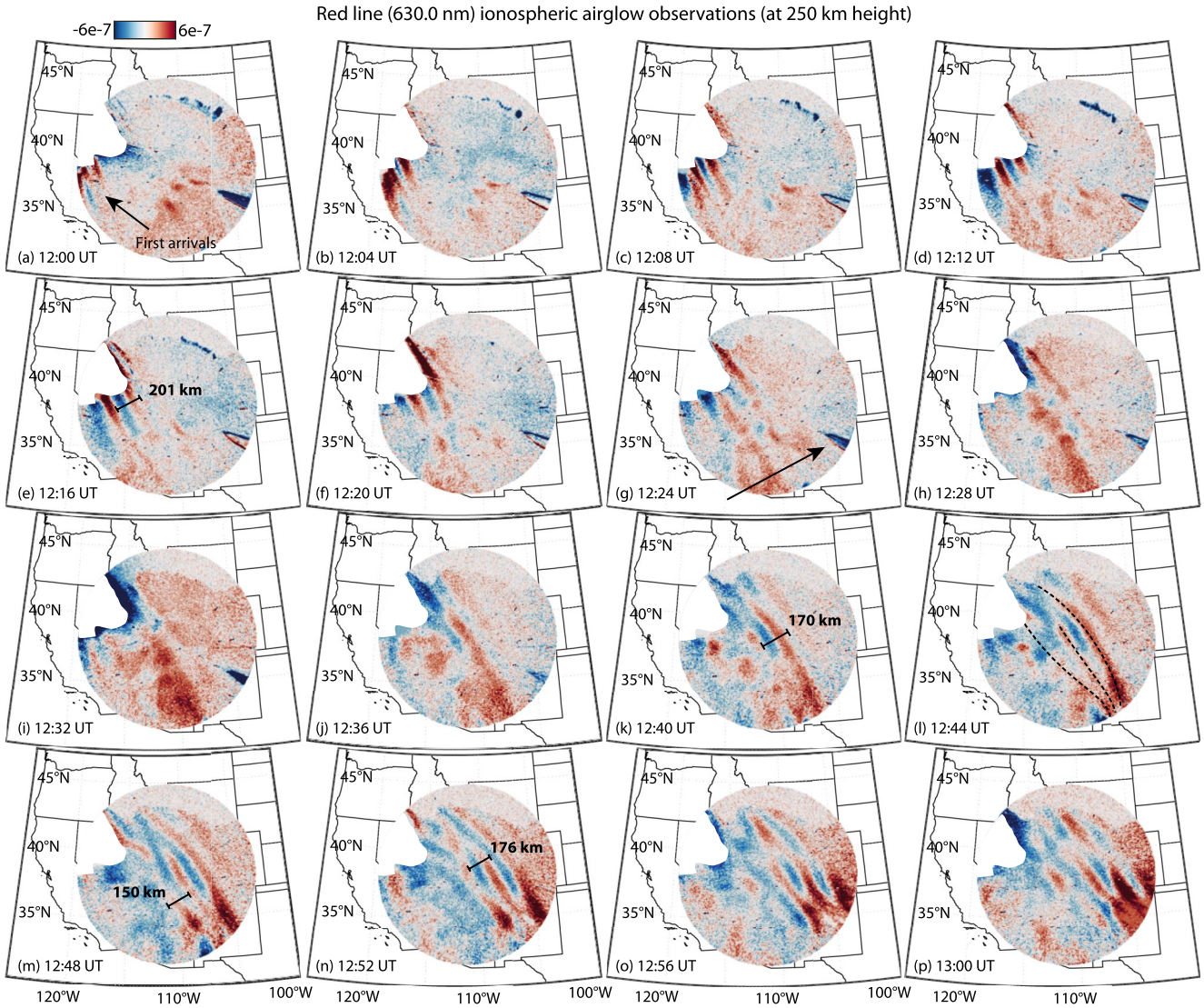

Figure 6. Ionospheric 630.0 nm red line emission observations. The difference images for 16 time epochs are unwarped onto the Continental United States map. The animation is provided in Movie S1.

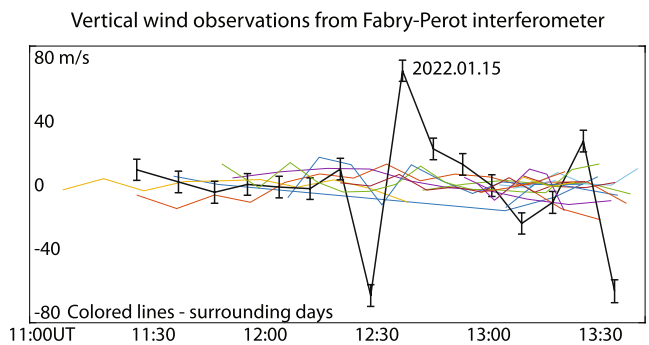

Figure 7. Fabry-Perot Interferometer measurements of vertical wind on 15 January and 19 days surrounding it.

Figure 7 collates time-series of vertical thermospheric winds measured with the FPI located at Lowell Observatory. Along with observations during 15 January, we plot data between 6 January and 15 February for comparison. All measurements that were taken during the same time of day, and pass the quality control criteria during this period (see Text S1.4 in Supporting Information S1), are plotted. During 15 January, the FPI detected large fluctuations of up to ∼130 m s^{-1} peak-to-peak, matching the time of arrival of the first packet of AGWs discussed earlier. Although the data set is limited in its sampling rate, the estimated periods of the identified fluctuations lie in the range 25–30 min. The latest samples on this plot at ∼13:30 UT are measured shortly before sunrise, which commonly yields larger errors. Otherwise, it can represent fluctuations related to the second packet of AGWs (discussed earlier based on surface pressure and GOES-16/17 satellite observations), having amplitudes of ∼75 m s^{-1} peak-to-peak. The observed fluctuations on the 15 January appear to be a large statistically significant anomaly relative to more typical profiles for other days.

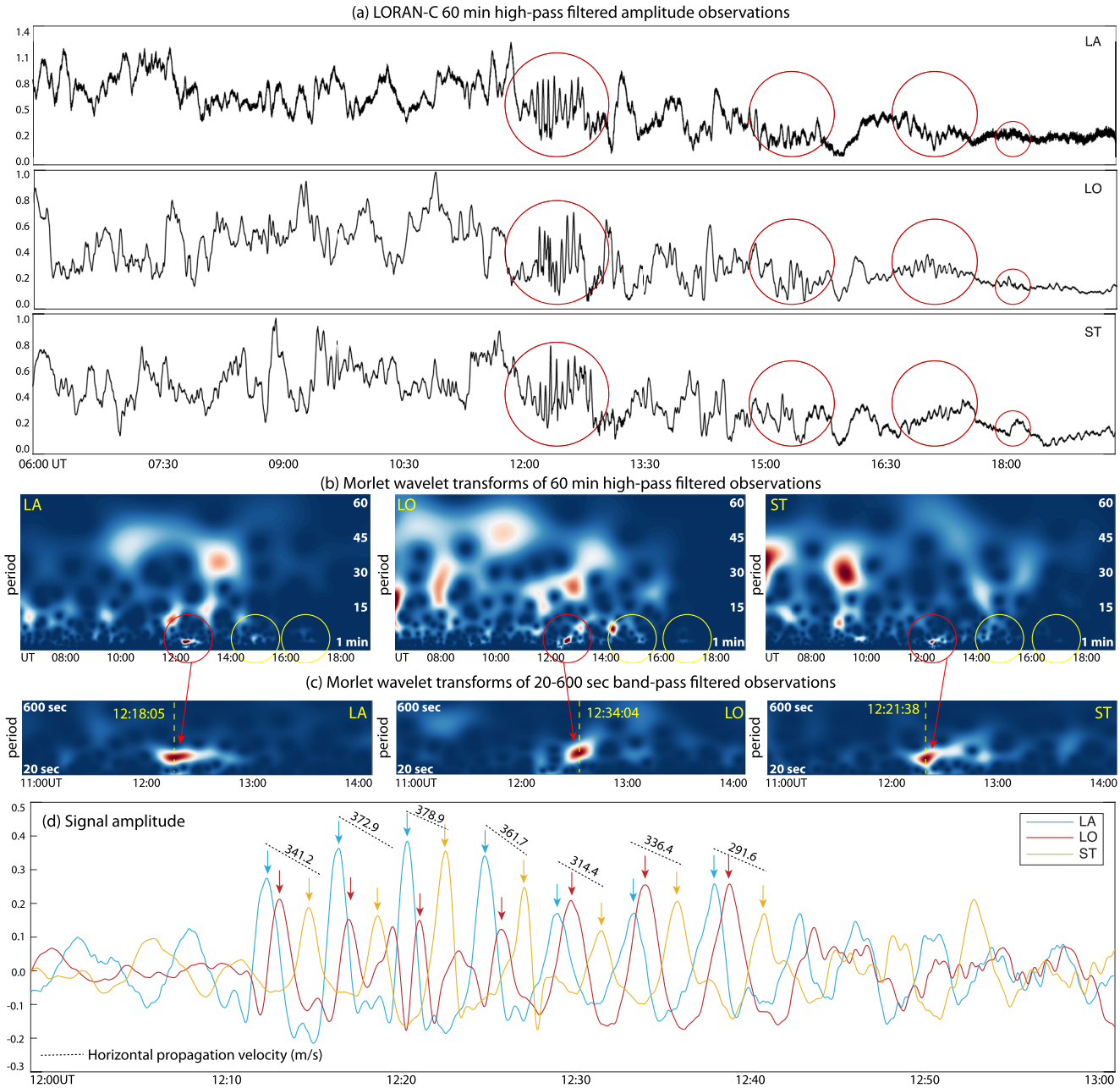

Figure 8. (a) Time-series of 60 min high-pass filtered signal amplitudes from Fallon LORAN-C campaign's stations Los Altos (LA), Lick Observatory (LO), and Stockton (ST). Morlet wavelet transforms of (b) 60 min high-pass and (c) 20–600 s band-pass filtered observations. (d) Time-series of 20–600 s band-pass filtered signal amplitude observations between 12:00 and 13:00 UT.

3.4. LORAN-C Experiment Observations

Figure 8a shows 60 min high-pass filtered signal amplitude observations derived from data acquired during the Fallon LORAN-C campaign from three receivers that operated during the 15 January. Two-hour high-pass filtered time-series are provided in Supporting Information S1 for comparison. Sets of short-period fluctuations can be discerned at ~12:20–12:50 UT, ~14:45–15:35 UT, ~16:40–17:30 UT, and ~18:30–19:00 UT. Leading fluctuations appear correlated among the three stations, and exhibit unusually large amplitudes and coherent short-period pulses of ~4.3 mHz or 3.8 min (Figure 8c), similar to those detected with the mesospheric 557.7 nm green line imager (cf. Figure 5). Later fluctuations, between ~14:45–15:35 UT and ~16:40–17:30 UT, also exhibited periods of 3–4 min, although of comparatively smaller amplitudes (Figures 8a and 8b).

Figure 8d focuses on the first packet of fluctuations, representing 20 s–10 min band-pass filtered amplitude observations from three receivers. These highly unusual and large amplitude fluctuations appeared at ∼12:10 UT, and lasted until ∼12:50 UT, thus overlying in time with fluctuations found in green line airglow observations. The shapes of signals illustrate coherence among all three receivers, whereas earlier or later fluctuations are not coherent at all. Based on the distance between reflection points (assumed here to be at 80 km altitude) of stations LA and ST (see Figure 1b), as well as identifying signal peaks as demonstrated in Figure 8b, we estimate the horizontal speed of propagation of fluctuations between these stations to be in the range of ∼342 ± 50 m s^{-1}. Biases that can affect the estimation of speeds include the non-planar geometry of phase fronts of TIDs propagating between reflection/observation points (rather than phase fronts assumed perpendicular to the direction between stations), possible superpositions of TIDs moving in different directions, and (to a lesser extent) the uncertainties of spatial coordinates and altitudes of reflection points.

3.5. GNSS Total Electron Content Observations

Figure 9 presents CONUS maps of vertical TEC (vTEC) processed with 10 min high-pass and 5–40 min band-pass filters. The animation for the full day of 15 January, which also includes vTEC processed with 60 and 120 min high-pass filters, are provided in Movie S6. The color scale ranges are selected to allow some saturation that helps to reveal the small-scale and weak-amplitude features.

The first packet of TIDs arriving at similar time as Lamb wave modes at the surface appeared over the southwest of CONUS at ∼11:40 UT (see the animation in Movies S1–S7). Long-period and large-scale fluctuations (300–1,000 km values of λ_x, 20–60 min periods) were followed by packets of short period ones (50–200 km values of λ_x and 3–10 min periods). The leading TIDs, propagating inland, coincided in time with a set of TIDs propagating toward the Pacific Ocean (this is seen clearly from the animation). Although initially TIDs appeared over the entire west coast (Figures 9a–9c), we find a similar pattern of TID amplitudes as discussed earlier based on surface pressure and GOES-16/17 satellite observations later at ∼13:00–14:00 UT. The fluctuations were mostly confined to the south of CONUS (>1 TECu in amplitude), while no (or very weak) fluctuations were observed at latitudes of ∼38–50°N (Figures 9c and 9d). Eventually, when TIDs to the south reached the eastern parts of CONUS after ∼14 UT, TEC fluctuations reappeared over the whole range of latitudes, but did not exhibit clear linear looking phase fronts, with fluctuations to the north lagging behind (Figures 9e and 9f). We note that some TIDs are detectable earlier than the largest amplitude TIDs which arrived at CONUS at ∼11:40 UT along with Lamb wave modes discussed here. The observations also include long-period fluctuations of ∼2 hr, appearing over the whole CONUS between 15 and 20 UT (Figure 10d).

The second clearly discernible packet of TIDs, propagating from the west to east over all latitudes, appeared at ∼14 UT (Figures 9e and 9f and the animation in Movie S6), similarly to fluctuations found in pressure observations at the surface (Figure 4a). These TIDs were of slightly shorter periods, from minutes to a couple of tens of minutes, and propagated until ∼22:30 UT (Figures 9i–9l). The only time window without coherent propagating TID dynamics was between 16 and 17:30 UT, with mostly chaotic patterns of TID fluctuations in different directions, some of them potentially not related to AGWs from the volcano eruptions (Figures 9g and 9h). We also point to a potential overlay of some TIDs generated by AGWs modulated in the upper atmosphere or evolving with Lamb wave modes, and TIDs generated by secondary gravity waves (Vadas et al., 2023a, 2023b), or gravity waves induced from tsunamis (Li et al., 2023; Pradipta et al., 2023), arriving earlier or later in time than Lamb wave modes. Overall, most of the amplitudes of TIDs lie in the range of 0.1–1 TECu, although some of the fluctuations reach values of ∼1.5 TECu. All of these amplitude values are well-above the noise floor.

To demonstrate v_ϕ and the arrival of several packets of TIDs, Figures 10a–10d include vTEC observations processed with 10 min high-pass, 5–40 min band-pass, 60 min high-pass and 120 min high-pass filters plotted as time-distance diagrams. The distances are calculated between ionospheric pierce point positions for each satellite-station pair and the volcano location at 20.55°S/175.385°W based on the Haversine formula. The estimated horizontal speeds of the leading TIDs arriving to CONUS at ∼11:40 UT along with Lamb wave modes, and which propagated through the whole range of distances, were in the range of 310–340 m s^{-1} (Figures 10b–10d). Most of the TIDs reaching the west coast of CONUS ∼2 hr after the first packet of TIDs propagated with comparable v_ϕ. A time-longitude diagram along 35°N is provided in Figure 10e to illustrate the TIDs propagating back

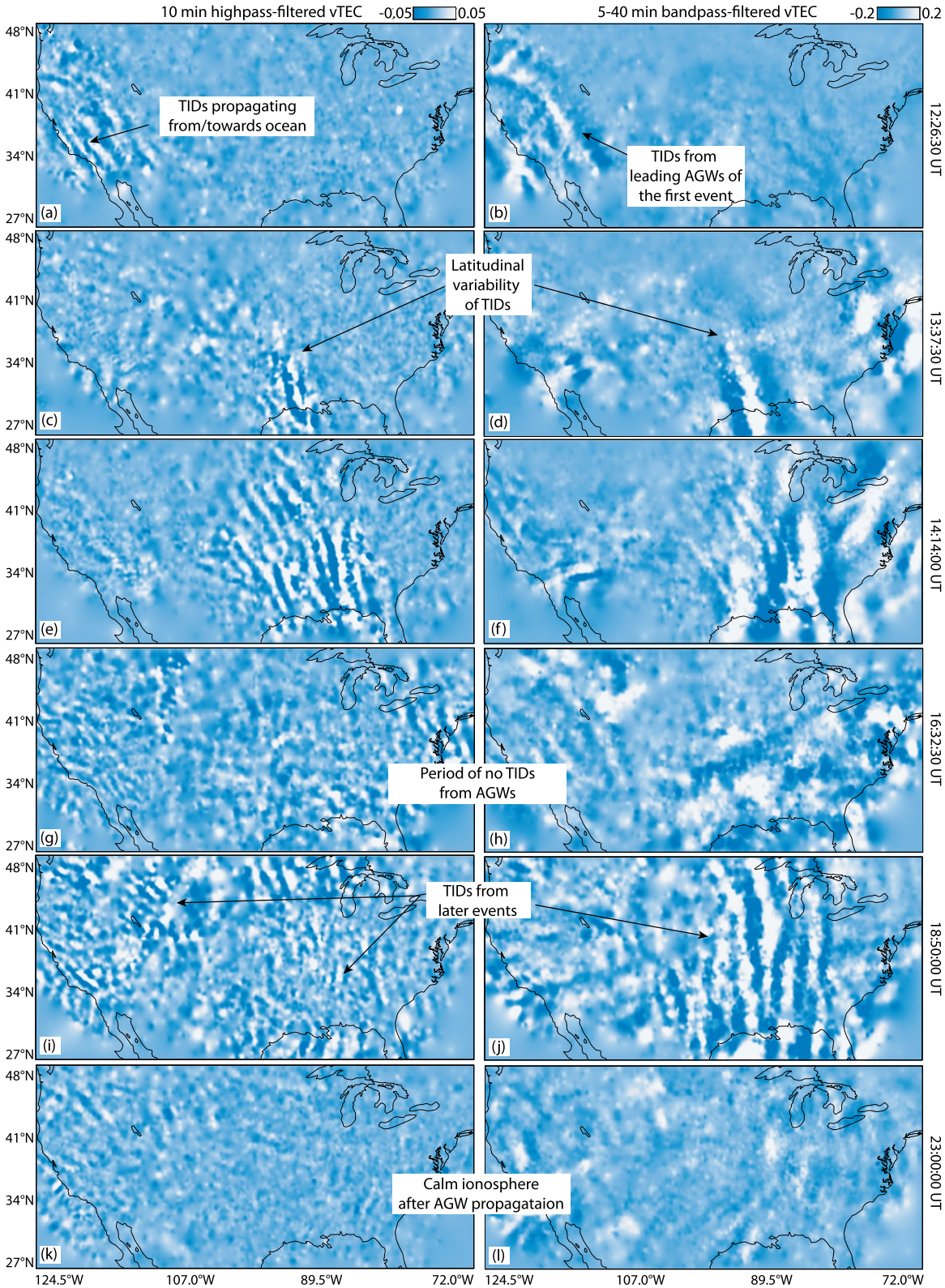

Figure 9. Six time epoch snapshots of gridded and mapped over Continental United States vTEC observations processed with 10 min high-pass (left column), 5–40 min band-pass (right column). The colorbars are oversaturated for better visibility of small scale and amplitude features.

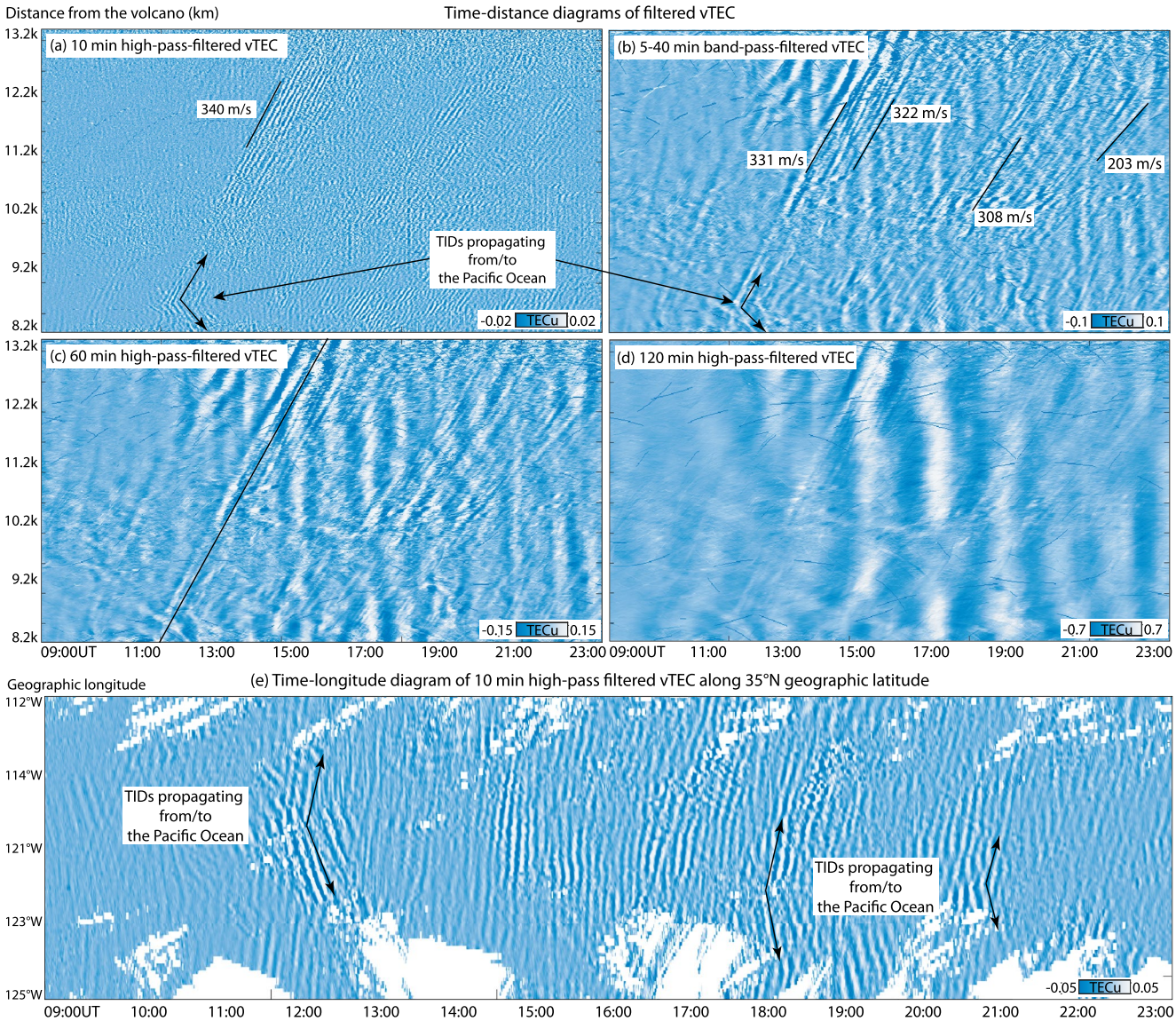

Figure 10. Time-distance diagrams of vTEC processed with (a) 10 min high-pass, (b) 5–40 min band-pass, (c) 60 min high-pass, and (d) 120 min high-pass filters over the distances of 8,200–13,200 km from the volcano position (20.55°S/175.385°W). (e) Time-longitude diagrams of 10 min high-pass filtered vTEC along 35°N. The colorbars are oversaturated for better visibility of small scale and amplitude features.

to the Pacific Ocean at the time of the leading TID arrivals at ~11:50 UT. For reference, we provide the same diagrams as Figure 10e, but for 14–18 January in Text S3.1 in Supporting Information S1 and we find no such dynamics during days other than 15 January. Similar TIDs were observed moving toward the ocean along with TIDs propagating to the east at ~18 UT and ~21 UT.

3.6. Multi-Observation Correlative Analysis of Fluctuations

To demonstrate the link between the volcano eruption sequence on the 15 January and times of excitation with propagation of AGWs and TIDs to and over CONUS, we performed a joint multi-instrument analysis of the observations. In Figure 11a, we provide time-distance diagrams of 180 min high-pass filtered ASOS surface pressure, GOES-17, LORAN-C LA receiver and 5–40 min filtered GNSS TEC observations, connecting fluctuation phase fronts to the volcano position with dashed black lines. To better constrain slopes of phase fronts, we incorporate barometer observations at Hawaii and microbarometer observations 64 km away from the Hunga Tonga volcano (21.1°S/175.2°W). GOES-17 data are used only for the quadrant northeast of the volcano position.

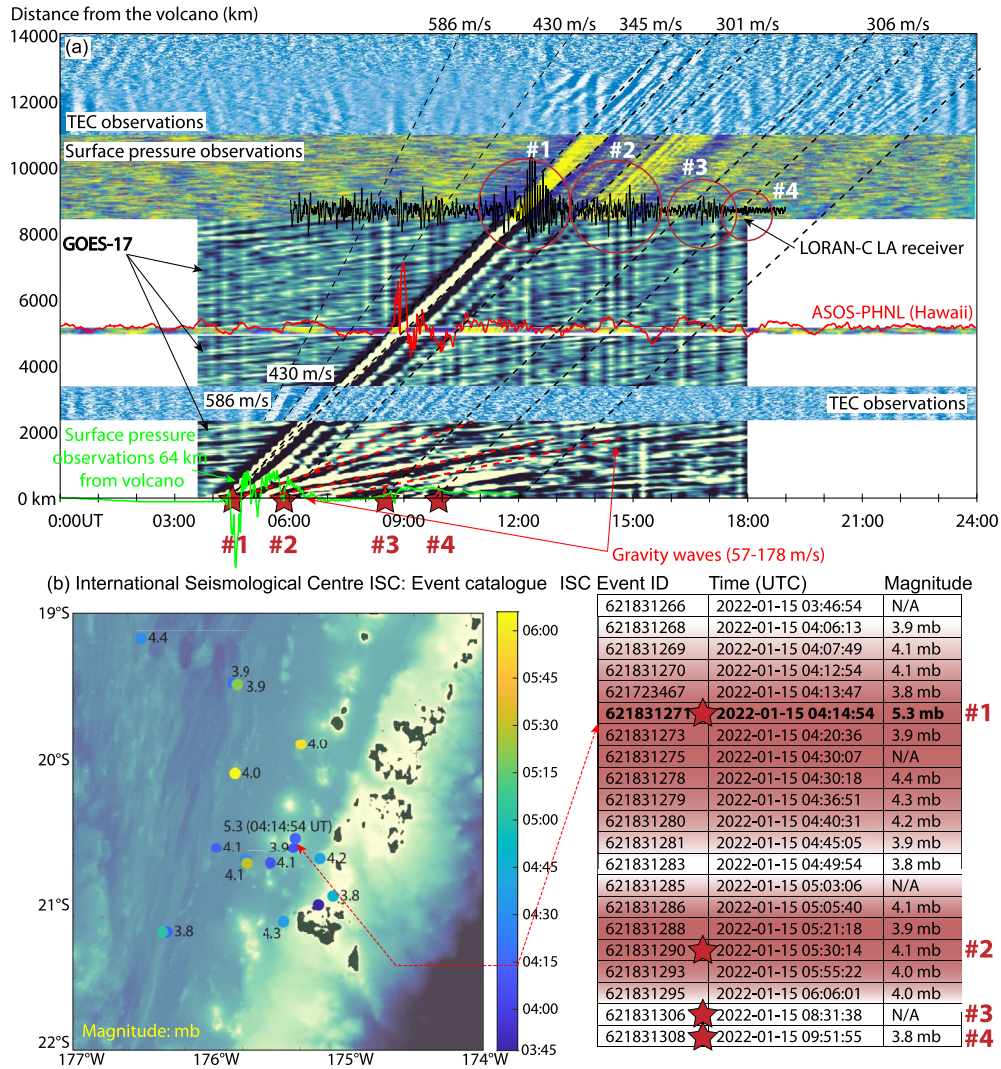

Figure 11. (a) Time-distance diagrams of surface pressure, GOES-17, total electron content and LORAN-C observations from the position of Hunga Tonga volcano to 14,000 km. The colorbars of figures are oversaturated for better visibility of phase-fronts. Red stars attribute to International Seismological Centre (ISC) catalog events. (b) Geographic locations of ISC catalog events to the left and their ISC IDs and estimated time epochs and magnitudes to the right.

Along with those over CONUS, we include TEC observations at distances of 2,500–3,500 km, although they are to the south of the volcano over New Zealand. Figure 11b presents the times, estimated locations and magnitudes of events in the vicinity of the volcano from the ISC Event catalog (Bondár & Storchak, 2011).

According to the ISC catalog, the main sequence of the events lasted for several hours from 03:46 to 09:51 UT. We find it hard to exactly link the first and second packet of AGWs discussed earlier with *specific* events from the ISC catalog, as AGWs and TIDs propagated with slightly different speeds depending on atmospheric state conditions and alignments and a finite time for wave generation. Based on our analysis of apparent horizontal speeds, the error in the estimation of excitation times is ±15 min. Instead, we separate events into two sequences, as depicted in Figure 11b via the red gradient shading, which are centered around the strongest event of magnitude 5.3 at 04:14:54 UT (Event #1) and the event of magnitude 4.1 at 05:30:14 UT (Event #2). We highlight that such separation is made for the convenience of the discussion, and because two discernible packets of fluctuations can be identified based on surface pressure and GOES-16/17 satellite observations. We note that the strongest event in the sense of seismic signal does not necessarily point to the strongest atmospheric response event, as was shown in Section 3.2.

We identify at least four sets of fluctuations that have coinciding onset times and comparable v_ϕ across the data set. The onset of the strongest fluctuations from the first packet with v_ϕ of ∼300–345 m s^{-1} closely matches the time of the Event #1 at ∼04:14 ± 15 min UT. Both phase fronts of v_ϕ of 301 and 345 m s^{-1} that we find based on surface pressure observations trace back to this time window. All demonstrated measurements suggest the strongest perturbations related to this set of AGWs and TIDs.

Back-tracing of the second packet of AGWs and TIDs toward the volcano position, which arrived ∼2 hr later at CONUS, provides its excitation time at 05:50 ± 0:15 UT. This time window matches a set of ISC-reported events (catalog's identification numbers (ID) 621731286/88/90/93/95) that occurred in the window of 05:05-06:06 UT, which we titled as Event #2. The GOES-17 observations have phase fronts that coincide with those from surface pressure measurements. LORAN-C and GNSS TEC observations demonstrate comparatively strong fluctuations at the time of arrival of AGWs from this event, too.

Next, we find surface pressure fluctuations arriving at CONUS at ∼15:30 UT, which match those from GOES-17 satellite observations, propagating with v_ϕ of 300–310 m s^{-1}. Again, LORAN-C and GNSS TEC observations reveal perturbations that coincide with those at the ground and in the troposphere in their times of arrival. Back-tracing of phase fronts to the volcano position suggests the time of excitation at ∼08:40 UT. The event from ISC catalog that is close to this time has ID 621831306 and occurred at 08:31:38 UT (we title it as Event #3), although its magnitude was not specified. Discernible fluctuations can also be seen at approximately the same time based on barometer data 64 km away from the volcano.

Finally, we highlight the fluctuations that were excited at ∼10 UT and find the event at 09:51 UT of magnitude 3.8 mb from the ISC catalog, which we mark as Event #4. Fluctuations for this event can be traced in all observations presented, except microbarometer observations at 64 km from the volcano, possibly due to a comparatively weak signal. Perturbations in GNSS TEC are less evident for this event too, plausibly due to the small amplitudes of related TIDs. In addition, tracking phase fronts from the GOES-17 satellite and surface pressure observations suggests another excitation time of AGWs at ∼12 UT, although we do not find a relevant event in ISC database.

GOES-17 observations also illustrate the excitation of a broad spectrum of gravity waves, propagating from the volcano position with v_ϕ of 57–178 m s^{-1}. We also point to the TEC observations at distances 2,500–3,500 km include fluctuations with v_ϕ of 430 and 586 m s^{-1} that can be tracked comparatively close to the source, thus we will not address them in detail. We, however, point to the study by Vadas et al. (2023b), who proposed secondary gravity waves to be the source of these TIDs.

4. Discussion

4.1. Spatial and Temporal Evolution of AGWs and TIDs

We summarize the rich spectrum of fluctuations measured with different instruments including their estimated periods and v_ϕ, as well as temporal and spatial resolutions of measurements in Table 1. The AGWs and resulting TIDs over CONUS exhibited periods from several to tens of minutes and v_ϕ in the range 295–392 m s^{-1} (corresponding to λ_x values of hundreds of kilometers). The pressure fluctuations from the strongest sequence of eruptions (Event #1) had a marked variability of v_ϕ, with the lower boundary of the range matching the average speeds of Lamb wave modes estimated, for example, by Carvajal et al. (2022) from ocean-based observations (∼307 m s^{-1}), while the upper boundary exceeded this speed by almost 40 m s^{-1}. Surface pressure fluctuations to the south of CONUS propagated with higher v_ϕ, whereas those to the north were lagging behind. At the same time, we do not find such variability of v_ϕ from the Event #1 over Alaska or the fluctuations related to the Event #2.

The analysis of 1-min GOES-16 regional observations reveal the presence of fluctuations of much smaller scales than reported earlier based on 10-min imagery (Winn et al., 2023; Wright et al., 2022). Our results are in agreement with Horvath et al. (2023) who suggested similar wavelengths and periods of fluctuations over CONUS and we refer to their study for the detailed analysis of 1-min GOES satellite observations over different mesoscale regions. Indeed, as demonstrated by Horvath et al. (2023) in detail, spatio-temporal aliasing of 10-min observations precludes the analysis of wavelengths and periods of fluctuations, yet are effective in attributing propagation over large distances. At the same time, the 1-min observations do not reveal vivid signatures of longer period fluctuations of tens of minutes, which are nevertheless found in surface pressure observations discussed

Table 1
Characteristics of Observed Atmospheric and Ionospheric Fluctuations and Resolution of Observations

#	Observations	T (min)	v_ϕ (m s^{-1})	Resolution of instrument
1.	Pressure at the surface over CONUS	5–50	301–345	1 min
2.	GOES-16/17 (troposphere):			
	Lamb wave modes over CONUS	3–8	300–330	1-min/∼2 km nadir/∼1,400 × 1,600 km
	Near-field gravity waves	40–90	57–178	10-min/∼2 km nadir, 83° local zenith angle
3.	LORAN-C (at 80 km height)	3–4	342 ± 50	2 s/∼20 km averaging region
4.	Mesopause airglow (at 95 km height)	∼5	295–330	2 min/∼1 km zenith/∼500 km FOV
5.	Imager Ionospheric airglow (at 250 km height)	∼9	320–335	4 min/∼3.5 km zenith/∼1,800 km FOV
6.	FPI Ionospheric airglow (at 250 km height)	∼25–30	N/A	8 min/10 × 10 km FOV
7.	Total electron content (∼200–350 km height):			
	2,000–3,500 km from the volcano	∼40	430–586	15/30 s
	Over CONUS	6–60	300–345	1 s

in this and other studies (e.g., Matoza et al., 2022; Vergoz et al., 2022). This may be a function of the sensitivity of GOES observables to those scales of interest; or, that the longer fluctuations (λ_x > 700 km) are not clearly constrained in the limited ∼1400 × 1600 km regions of the 1-min mesoscale observations.

Lamb wave mode ray-tracing modeling results within both NAVGEM and NRLMSISE-00/HWM-14 background atmospheric environments suggest that speed variability to the south and north of CONUS is explained by the inhomogeneity of the atmosphere's winds. Nevertheless, our simulations do not explain some substantially faster propagating phase fronts with speeds of ∼345 m s^{-1}, suggesting variation of Lamb wave mode group speeds in the range 307–321 m s^{-1} over CONUS. Although the simulations with constant speed approximation serve as a good starting point (Amores et al., 2022; Kubota et al., 2022), Lamb wave mode propagation in an inhomogeneous and stratified atmosphere over large distances may be more complex (including presence of multiple modes), leading to differences in their speeds and arrival times. Indeed, although the difference between ray arrivals and arrivals of fluctuations in surface pressure and GOES-16/17 observations can be considered negligibly small at locations comparatively close to the volcano, the error accumulates with distance and reaches several degrees over CONUS from simulations based on global empirical models NRLMSISE-00 and HWM-14. The non-spherical nature of the Earth, as well as nonlinear effects, which are not considered here, can result in ray arrival discrepancies between the simulations and observations.

Next, we note that the mesospheric airglow and LORAN-C fluctuations exhibit comparable periods of 3–5 min, which is not surprising as they both reveal fluctuations at similar altitudes near the mesopause. However, their v_ϕ are faster than the typically-expected speed of sound at 80–95 km altitude of ∼265–286 m s^{-1} (here, calculated based on NRLMSISE-00 model for the position 32.715°N/62.83°W), and thus appear to be similar to Lamb wave modes or related AGWs evolving with them vertically rather than infrasound. Neither observations include clear evidence of long-period fluctuations (∼6–60 min) unambiguously connected to other AGW arrivals, as found from observations below (ground pressure) or above (FPI, TEC measurements). To some extent, this may be connected with the nuances of observational techniques, but also may be consistent with the vertical evolution of AGW fluctuations that become evanescent at mesopause altitudes while nevertheless tunneling some energy into the thermosphere (e.g., Heale et al., 2022).

Ionospheric airglow observations from the imager at Capitol Reef Field Station (although unable to investigate long-period fluctuations due to the short window of available data before the sunrise) captured short period fluctuations of ∼9 min, which are also present in TEC. At the same time, the FPI observations of ionospheric airglow at Lowell Observatory detected longer period fluctuations of 25–30 min. Signal aliasing from the evolving AGWs, as well as the potential for net nonlinear impacts of the AGWs on the thermosphere-ionosphere system, may also explain features of these FPI observations. Regardless of sensitivity limitations of airglow imager and FPI observations, the observations all clearly demonstrate the arrivals of large amplitudes fluctuations at ∼12 UT, along with fluctuations found in measurements of other instruments.

The appearance of packets of TIDs from the Event #2 seen in TEC observations at ∼14 UT, also agrees temporally with the arrival of the direct tsunami to the west coast of the United States (Carvajal et al., 2022). Tsunamis can generate packets of AGWs of a broad range of periods and spatial scales, propagating with faster or slower v_ϕ than the tsunami itself or Lamb wave modes, and drive detectable TIDs (Inchin et al., 2020; Munaibari et al., 2023; Vadas et al., 2015). Thus, we cannot exclude the possibility that the reported sets of TEC fluctuations represent a superposition of TIDs from different sources, including, for example, gravity waves from the direct tsunami generated over the volcano (Carvajal et al., 2022) or via coupling from the tsunami generated by Lamb wave modes (Kubota et al., 2022), or other primary and secondary gravity waves excited over the volcano that propagated globally (Vadas et al., 2023b). At the same time, based on the analysis of estimated ocean surface vertical displacements (e.g., https://nctr.pmel.noaa.gov/tonga20220115/), we do not expect that these (weak) tsunamis generated the dominant TID signals in the ionosphere that were tracked over CONUS from the west to east (Inchin et al., 2020, 2022). Additionally, although our analysis is focused on 15 January, we also reference S.-R. Zhang et al. (2022), who demonstrated TIDs during 16 and 17 January over CONUS, which exhibited comparable v_ϕ and periods as discussed here, propagating apparently outbound and inbound radially along great circles.

Although not directly related to the discussion of packets of AGWs and TIDs investigated in this paper, we would like to point to several interesting observed phenomena. First are AGWs that propagated with v_ϕ of 240–270 m s^{-1}, which we find in GOES-16/17 and TEC observations. Although some publications attribute them to fast internal gravity waves or secondary gravity waves (Vadas et al., 2023a; Wright et al., 2022), others suggest other modes, such as the so-called Pekeris mode (Watanabe et al., 2022), or an L1 Lamb pseudomode, which have comparable speeds of ∼254 m s^{-1} (Francis, 1973, and references cited therein). We do not find fluctuations clearly traceable in pressure observations propagating with v_ϕ of 240–270 m s^{-1}. This may indicate that they exhibit different vertical modal structure as they are guided by the atmosphere, or that they were of small amplitudes and overlaid by stronger fluctuations driven by AGWs in the second packet.

Some TIDs at distances of ∼2,000–3,500 km from the volcano location had periods of ∼40 min and propagated with v_ϕ of 430–583 m s^{-1}. They were faster than the TIDs associated with signals in the lower atmosphere (see Figure 11), but slower than what would be expected for TIDs induced by directly-arriving acoustic shocks at the bottom of ionospheric F layer at 200–300 km altitude (∼700–900 m s^{-1}). Tracking of their v_ϕ toward CONUS, may suggest possible consistency in fluctuations albeit with uncertain continuity in their phase fronts at ∼8–10 UT at distances ∼12,000–13,000 km. We also note that the fluctuations at 2,000–4,000 km are to the south of the Tonga eruption, collected in New Zealand, and not those propagating to CONUS. We cannot effectively trace these phase fronts from the volcano location toward CONUS as the spatial gap between them is too large (∼9,000 km), nor confirm their continuity with observations over CONUS. Thus, we defer drawing conclusions on the source of these TIDs seen at distances 2,500–3,500 km and TEC fluctuations observed at a range of distances over CONUS at ∼8–10 UT, but highlight the study by Vadas et al. (2023a, 2023b) who suggest secondary gravity waves as their sources.

We note TIDs of ∼2 hr periods, as demonstrated in Section 3.5 with regards to Figure 10d. While the 2-hr plasma fluctuations associated with these larger-scale TIDs could have a connection with volcano eruptions and their impacts on the atmosphere and ionosphere (along with inducing a consequent ionospheric electrodynamic effect), they could also be of another nature, for example, a response to the geomagnetic storm that occurred on the 14 January.

4.2. Amplitude Variability of AGWs and TIDs

The propagation of AGWs from the first packet exhibited substantial meridional variability of amplitudes over CONUS, which we find in surface pressure data, GOES-16/17 imagery, and also consistently in ray-tracing simulation results. We note that similar variability is also found in TIDs from TEC observations. Although the fluctuations along the whole west coast of United States had comparable amplitudes, the strongest fluctuations propagated to the south and north of CONUS, farther inland to the east, and substantially smaller amplitudes were detected in the mid-latitudes of CONUS. Both long- and short-period surface pressure fluctuations exhibited this non-uniformity in their observed amplitudes, and the Lamb wave mode ray-tracing simulation results including atmospheric and wind specifications from the NAVGEM reanalysis products help to clarify this effect. The rays are markedly deflected by horizontal winds, such that rays are focused (increased density of rays) to the north and

south of CONUS, leading to defocusing (reduced density of rays) over the mid-latitudes of CONUS. We also point to the simulation of Lamb wave modes with WACCM-X model by H.-L. Liu et al. (2023), which seems to demonstrate this meridional variability of amplitudes of fluctuations (e.g., see their Figure 3a and provided animation).

This consistent variability of amplitudes of atmospheric and ionospheric fluctuations, of comparable periods and v_ϕ, suggests that their fluctuation fields evolved together with the Lamb wave modes in lower atmospheric data, and correlate clearly with their signals observed over CONUS. We note that secondary gravity waves have also been suggested as a source of ionospheric disturbances as demonstrated by Huba et al. (2023); Vadas et al. (2023a), however we do not find sufficient agreement between observations of fluctuations at ∼12 UT and these modeling results in speeds nor timing. Instead, our findings are far more consistent with the reports of global Lamb wave mode propagation demonstrated by H.-L. Liu et al. (2023). We also note that the ray simulations using NAVGEM environment data markedly improve the agreement with observations, contrasting with ray-tracing in global empirical model data from NRLMSISE-00 and HWM-14, which further supports this interpretation that the Lamb wave modes and related AGW (including evanescent) vertical coupling contributed to the fluctuations observed at all altitudes.

We highlight the amplitudes of vertical winds driven by AGWs that we find from FPI observations of up to 130 m s^{-1}, even though under-sampled. The amplitudes are indeed extreme, while 19 days surrounding the event demonstrate amplitudes in the range not exceeding ∼30 m s^{-1}, although the data are limited in sampling resolution to assess the full spectrum of underlying waves. The amplitudes are comparable with horizontal wind fluctuations reported earlier based on, for example, SuperDARN Radar observations over CONUS (J. Zhang et al., 2022). Such winds can indicate wave effects resulting in a marked redistribution of plasma and generation of large dynamo effects and equatorial anomalies, for example, equatorial electrojet of amplitudes reaching 0.2 A/m observed with SWARM satellite (Harding et al., 2022) and uniquely deformed equatorial ionospheric anomaly crests observed with GNSS TEC (Aa et al., 2022b).

Along with the inhomogeneous atmospheric state and winds (likely even to a greater extent than captured in ray-tracing simulations) and nonlinear wave propagation away from the sequence of eruptive events, the reflection and scattering of AGWs propagating over the Sierra-Nevada and Rocky mountain ranges could also contribute to the variability of fluctuation amplitudes. Earlier, the reflection of Lamb wave modes from the Andes was reported based on GOES-16 observations (Wright et al., 2022). Although we do not find reflected AGWs in GOES-16/17 data from mountains over CONUS (plausibly due to smaller scales of mountains over CONUS and thus comparatively small amplitudes of reflected AGWs), we find fluctuations in GNSS TEC data that propagated toward the Pacific Ocean at the time of the arrival of the first packet of TIDs. We speculate that the complexity of signals (especially at shorter periods) in LORAN-C observations, although consistent between stations, can also be a result of fluctuations induced by scattered waves propagating vertically and/or in different directions above the evolving Lamb wave modes and accompanying AGWs. We expect that the topography primarily affected the propagation of comparatively shorter-period Lamb wave modes and AGWs, in contrast to the propagation of longer-period Lamb wave modes that exhibited comparable or larger wavelengths than the scales of topographical features.

Likewise, excited Lamb wave modes differ in their sources and thus in their periods and amplitudes. Although Lamb wave modes are not dispersive to first-order approximation (Bretherton, 1969), their nonlinear propagation and interact in an inhomogeneous stratified atmosphere with varying winds will further contribute to their apparent variability over CONUS. Propagating along with the dominant spectral components were short-period fluctuations of ∼3–10 min, which can also relate to shorter-period Lamb wave modes, but also include infrasound near the acoustic cut-off frequency, which may be excited locally from Lamb wave mode scattering and interaction with topographic features yielding λ_x values ranging from tens to a couple of hundred kilometers.

4.3. Identifying a Set of Eruptive Events

The multi-instrument analysis of observations reveals at least four distinct packets of fluctuations, arriving to CONUS at ∼11:40 UT, 13:40 UT, 15:30 UT, and 17:30 UT. The gaps between arrival times, as well as the consistency of their estimated excitation times with several events at ∼4:14–4:40 UT, 5:05–6:06 UT, 8:31 UT,

and 09:51 UT, based on the ISC event catalog, suggest that AGWs could be excited during distinct episodes (cf. Figure 11). The majority of previous studies were focused on the main eruptive Event #1 at 4:14 UT, but the large Event #3 at 8:31 UT, as found here, was also reported based on brightness temperature observations of the umbrella clouds with the Himawari-8 satellite (Gupta et al., 2022), as well as IMS infrasound station measurements (Matoza et al., 2022). Gupta et al. (2022) also reported the formation of two umbrella clouds within 1.5 hr of each other, which supports our conclusion of the excitation of the second-strongest packet of AGWs during Event #2.

These and additional eruption events are identified based on surface pressure, GOES-16/17 imagery, Fallon, NV, LORAN-C receptions, and TEC observations, which altogether support the conclusions. Thus, this is a demonstrative example of the possibility to identify and further-constrain very large, discrete, eruption events based on a set of independent atmospheric and ionospheric observations, even at far-fields. It also points to the applicability of such measurement techniques for the temporal and spatial localization of other impulsive natural and anthropogenic hazards, for example, large-magnitude earthquakes, tsunamis, rocket launches and other events that generate sufficiently strong AGWs in the atmosphere and TIDs in the ionosphere as well as in the solid Earth and ocean.

5. Conclusion and Future Work

Atmospheric and ionospheric fluctuations from AGWs generated by a sequence of Hunga Tonga-Hunga Ha'apai volcano eruptions on 15 January 2022 have been investigated. We focus on the properties of Lamb wave modes and accompanying AGW fluctuations over the Continental United States (CONUS), which is well-covered by various instruments in dense sensor networks as well as unique instruments operated by the authors. We analyzed surface-level pressure, tropospheric radiance observations with GOES-16/17 satellites, GNSS total electron content (TEC) and LORAN-C ionospheric D-region measurements, as well as mesospheric and ionospheric airglow and thermospheric FPI winds. These analyses are complemented by Lamb wave mode ray-tracing simulations, based on specifications of atmospheric state and winds from global empirical models NRLMSISE-00 and HWM-14 and deep-atmosphere meteorological reanalysis products generated by DA experiments using NAVGEM.

The dominant signatures measured at multiple altitudes above CONUS indicate the propagation and evolution of a broad spectrum of AGWs and TIDs, which accompany the passage of the Lamb wave modes at lower altitudes. Inhomogeneous stratification of the atmosphere, winds, and topography, as well as the sequence of potentially anisotropic sources of nonlinearly interacting AGWs, contributed to the overall complexity of wave fluctuation fields that were observed. Our ray-tracing simulation results, in particular with the specification of atmospheric state and winds from NAVGEM DA, support our conclusions on the propagation and modulation of Lamb wave modes in the lower atmosphere, revealing similar variability of ray speeds and their focusing over North America. Finally, based on back-tracing of phase fronts across multiple instruments and data sets, we identified several packets of arriving AGWs and TIDs, which appear discretely as having been excited by at least four separate sets of eruption events.

As the dominant signals detected throughout the depth of the atmosphere follow and correlate with the arrival of Lamb wave modes, they also demonstrate the importance of capturing the fully-compressible and nonlinear wave responses of the global atmosphere during and after events of this scale, to cover short-period dynamics as waves evolve over large regions. The apparent variability of the characteristics of fluctuations driven by AGWs and TIDs, at different altitudes, as well as in different packets, reveals the need for future improvements in observation techniques and modeling capabilities; these should be complemented with further theoretical investigations of nonlinear AGW dynamics in a stratified media, including their coupling with oceans.

We reiterate that our study is devoted to the investigation of fluctuations, with periods from minutes to tens of minutes, that arrived at CONUS together with the Lamb wave modes traceable from pressure observations at the surface and GOES-16/17 satellite imagery. Due to the spatial and temporal limitations of observations investigated, we do not address all aspects of variability nor all observed fluctuations, for example, those at longer (hours) periods and thousands of km of horizontal spatial scales that may also be present (Harding et al., 2022). Although not affecting our conclusions, we would like to note that these fluctuations could potentially results as effects

from primary or secondary gravity waves, generated by atmospheric sources (Li et al., 2023; Vadas et al., 2023b), or by forcing from direct tsunami or tsunami evolving with Lamb wave modes (Munaibari et al., 2023; Pradipta et al., 2023).

As with other studies in response to the Hunga Tonga-Hunga Ha'apai volcano eruptions on 15 January 2022, which have already provided advances in our understanding of NH wave dynamics and effects (e.g., H.-L. Liu et al., 2023; Matoza et al., 2022; Vadas et al., 2023b; Vergoz et al., 2022; Wright et al., 2022), we reiterate and summarize the need for continued efforts in the future to understand global short-period wave dynamics. Some directions for future investigations, including some also proposed earlier by others, include efforts toward:

1. Improved understanding of wave source processes; in particular, how the different atmospheric modes are generated and coupled in solids, oceans and the atmosphere;
2. Understanding how atmospheric waves, in particular the Lamb wave and other AGWs, propagate through a spatially and temporally variable deep atmospheres over topography, in realistic specifications of the atmospheric meteorological state and winds;
3. Appreciation of the nonlinear effects on wave signals recorded at large distances, and a better understanding of nonlinear effects on the vertical evolutions of AGWs, for example, as they are measured at different altitudes;
4. Quantification of AGWs and their effects on various layers, for the purpose of understanding them as diagnostics of wave sources and for quantitative assessments of NH magnitudes or severity (e.g., tsunami risks), as well as future opportunities to define instrumented observational techniques;
5. The synthesis of instrument observables for the propagation of AGW modes of different scales, from minutes to tens-of-minutes, and from ground to the upper atmosphere.

The efforts highlighted above, among others, require substantial and in some cases transformative improvements in modeling and observational/analysis capabilities. We look forward to sustained interdisciplinary collaborations to expedite and advance future studies.

Conflict of Interest

The authors declare no conflicts of interest relevant to this study.

Data Availability Statement

ASOS's barometer measurements used in our studies are post-processed datasets by Iowa Environment Mesonet system that can be found here: https://mesonet.agron.iastate.edu/request/asos/1min.phtml. 10-min GOES-16/17 satellite observations are downloaded using NOAA's Comprehensive Large Array-Data Stewardship System CLASS: https://www.avl.class.noaa.gov/saa/products/welcome. 1-min GOES-16 observations are available at AWS Open Data description page: https://registry.opendata.aws/noaa-goes/. We would like to thank the local team that manages the microbarometer station in Tonga for providing the pressure data shown in Figure 11, and to Corwin Wright for forwarding the data on to us. Global Navigation Satellite System observations in RINEX format were downloaded from The Geodetic Facility for the Advancement of Geoscience (GAGE) Data Server (https://www.unavco.org/data/gps-gnss/gps-gnss.html), The Crustal Dynamics Data Information System (CDDIS) (https://cddis.nasa.gov/Data_and_Derived_Products/GNSS/daily_30second_data.html), National Oceanic and Atmospheric Administration (https://geodesy.noaa.gov/CORS/data.shtml) and The Scripps Orbit and Permanent Array Center SOPAC (http://sopac-old.ucsd.edu/dataBrowser.shtml). Software for both the data transport system that retrieves data from the MANGO images and the processing pipeline are available at https://github.com/mangonetwork. These are all licensed under GNU General Public License v3.0. Raw MANGO imaging data are available at https://data.mangonetwork.org/data/transport/mango/archive/. Processed FPI data (winds, emission rates, uncertainties and quality flags) are publicly available from the Madrigal database (http://cedar.openmadrigal.org/).

Acknowledgments
The research was supported by DARPA Cooperative Agreement HR00112120003. This work is approved for public release; distribution is unlimited. The content of the information does not necessarily reflect the position or the policy of the Government, and no official endorsement should be inferred. Work at the University of California, Berkeley is supported through NSF award AGS-193307, at SRI International is supported through NSF award AGS-1933013, and at the University of Illinois is supported through NSF award AGS-1932953. NRL's research was supported by the DARPA AtmoSense program, and NRL's NAVGEM reanalysis runs were made possible by the DoD High-Performance Computer Modernization Program via grants of computer time at the Navy DoD Supercomputing Resource Center. S. A. Cummer would like to thank the Albright family, H. U. Frey, and D. M. Smith for their support in operating the LF sensors. Except Inchin P.A., all authors are listed alphabetically.

References

Aa, E., Zhang, S.-R., Erickson, P. J., Vierinen, J., Coster, A. J., Goncharenko, L. P., et al. (2022a). Significant ionospheric Hole and equatorial plasma bubbles after the 2022 Tonga volcano eruption. *Space Weather*, *20*(7), e2022SW003101. https://doi.org/10.1029/2022SW003101

Aa, E., Zhang, S.-R., Wang, W., Erickson, P. J., Qian, L., Eastes, R., et al. (2022b). Pronounced suppression and X-pattern merging of equatorial ionization anomalies after the 2022 Tonga volcano eruption. *Journal of Geophysical Research: Space Physics*, *127*(6), e2022JA030527. https://doi.org/10.1029/2022JA030527

Amores, A., Monserrat, S., Marcos, M., Argüeso, D., Villalonga, J., Jordà, G., & Gomis, D. (2022). Numerical simulation of atmospheric lamb waves generated by the 2022 Hunga-Tonga volcanic eruption. *Geophysical Research Letters*, *49*(6), e2022GL098240. https://doi.org/10.1029/2022GL098240

Assink, J. D., Averbuch, G., Smets, P. S. M., & Evers, L. G. (2016). On the infrasound detected from the 2013 and 2016 DPRK's underground nuclear tests. *Geophysical Research Letters*, *43*(7), 3526–3533. https://doi.org/10.1002/2016GL068497

Assink, J. D., Waxler, R., Lonzaga, J., & Frazier, G. (2012). Infrasound as a remote sensing technique for the upper atmosphere. *Journal of the Acoustical Society of America*, *132*(3), 2074. https://doi.org/10.1121/1.4755648

Astafyeva, E., Maletckii, B., Mikesell, T. D., Munaibari, E., Ravanelli, M., Coisson, P., et al. (2022). The 15 January 2022 Hunga Tonga eruption history as inferred from ionospheric observations. *Geophysical Research Letters*, *49*(10), e2022GL098827. https://doi.org/10.1029/2022GL098827

Astafyeva, E., & Shults, K. (2019). Ionospheric GNSS imagery of seismic source: Possibilities, difficulties, and challenges. *Journal of Geophysical Research: Space Physics*, *124*(1), 534–543. https://doi.org/10.1029/2018JA026107

Azeem, I., Yue, J., Hoffmann, L., Miller, S. D., Straka, W. C., III, & Crowley, G. (2015). Multisensor profiling of a concentric gravity wave event propagating from the troposphere to the ionosphere. *Geophysical Research Letters*, *42*(19), 7874–7880. https://doi.org/10.1002/2015GL065903

Bhatt, A. N., Harding, B. J., Makela, J. J., Navarro, L., Lamarche, L. J., Valentic, T., et al. (2023). Mango: An optical network to study the dynamics of the earth's upper atmosphere. *Journal of Geophysical Research: Space Physics*, *128*(10), e2023JA031589. https://doi.org/10.1029/2023JA031589

Bondár, I., & Storchak, D. (2011). Improved location procedures at the international seismological centre. *Geophysical Journal International*, *186*(3), 1220–1244. https://doi.org/10.1111/j.1365-246X.2011.05107.x

Bretherton, F. (1969). Lamb waves in a nearly isothermal atmosphere. *Quarterly Journal of the Royal Meteorological Society*, *95*(406), 754–757. https://doi.org/10.1002/qj.49709540608

Brown, P. G., Whitaker, R. W., ReVelle, D. O., & Tagliaferri, E. (2002). Multi-station infrasonic observations of two large bolides: Signal interpretation and implications for monitoring of atmospheric explosions. *Geophysical Research Letters*, *29*(13), 14-1–14-4. https://doi.org/10.1029/2001GL013778

Carvajal, M., Sepúlveda, I., Gubler, A., & Garreaud, R. (2022). Worldwide signature of the 2022 Tonga volcanic tsunami. *Geophysical Research Letters*, *49*(6), e2022GL098153. https://doi.org/10.1029/2022GL098153

Chunchuzov, I., Kulichkov, S., Popov, O., & Perepelkin, V. (2023). Evolution of the atmospheric pressure signal from the Tonga volcano with distance from it. *Izvestiya, Atmospheric and Oceanic Physics*, *59*(1), 1–15. https://doi.org/10.1134/s0001433823010024

Drob, D. P., Emmert, J. T., Meriwether, J. W., Makela, J. J., Doornbos, E., Conde, M., et al. (2015). An update to the Horizontal Wind Model (HWM): The quiet time thermosphere. *Earth and Space Science*, *2*(7), 301–319. https://doi.org/10.1002/2014EA000089

Eckermann, S. D. (2023). Augmented non-LTE parameterization of NO infrared radiative cooling rates. *Journal of Geophysical Research: Space Physics*, *128*(2), e2022JA030956. https://doi.org/10.1029/2022JA030956

Eckermann, S. D., Barton, C. A., & Kelly, J. F. (2023). Adaptation of θ-based dynamical cores for extension into the thermosphere using a hybrid virtual potential temperature. *Monthly Weather Review*, *151*(8), 1937–1955. https://doi.org/10.1175/MWR-D-22-0320.1

Eckermann, S. D., Ma, J., Hoppel, K. W., Kuhl, D. D., Allen, D. R., Doyle, J. A., et al. (2018). High-altitude (0–100 km) global atmospheric reanalysis system: Description and application to the 2014 Austral winter of the deep propagating gravity wave experiment (DEEPWAVE). *Monthly Weather Review*, *146*(8), 2639–2666. https://doi.org/10.1175/MWR-D-17-0386.1

Edwards, W., & Hildebrand, A. (2004). Supracenter: Locating fireball terminal bursts in the atmosphere using seismic arrivals. *Meteoritics & Planetary Sciences*, *39*(9), 1449–1460. https://doi.org/10.1111/j.1945-5100.2004.tb00121.x

Emmert, J. T., Drob, D. P., Picone, J. M., Siskind, D. E., Jones, M., Jr., Mlynczak, M. G., et al. (2021). NRLMSIS 2.0: A whole-atmosphere empirical model of temperature and neutral species densities. *Earth and Space Science*, *8*(3), e2020EA001321. https://doi.org/10.1029/2020EA001321

Fox, J. E. (2006). *Performance study of the LORAN-C system in the presence of wideband interference. Master's Thesis*. University of Tennessee.

Francis, S. H. (1973). Acoustic-gravity modes and large-scale traveling ionospheric disturbances of a realistic, dissipative atmosphere. *Journal of Geophysical Research*, *78*(13), 2278–2301. https://doi.org/10.1029/JA078i013p02278

Garrett, C. J. R. (1969). Atmospheric edge waves. *Quarterly Journal of the Royal Meteorological Society*, *95*(406), 731–753. https://doi.org/10.1002/qj.49709540607

Godin, O. A. (2012). Acoustic-gravity waves in atmospheric and oceanic waveguides. *Journal of the Acoustical Society of America*, *132*(2), 657–669. https://doi.org/10.1121/1.4731213

Gupta, A. K., Bennartz, R., Fauria, K. E., & Mittal, T. (2022). Eruption chronology of the December 2021 to January 2022 Hunga Tonga-Hunga Ha'apai eruption sequence. *Communications Earth & Environment*, *3*(1), 1–10. https://doi.org/10.1038/s43247-022-00606-3

Gusman, A. R., Tanioka, Y., MacInnes, B. T., & Tsushima, H. (2014). A methodology for near-field tsunami inundation forecasting: Application to the 2011 Tohoku tsunami. *Journal of Geophysical Research: Solid Earth*, *119*(11), 8186–8206. https://doi.org/10.1002/2014jb010958

Harding, B. J., Chau, J. L., He, M., Englert, C. R., Harlander, J. M., Marr, K. D., et al. (2021). Validation of ICON-MIGHTI thermospheric wind observations: 2. Green-line comparisons to specular meteor radars. *Journal of Geophysical Research: Space Physics*, *126*(3), e2020JA028947. https://doi.org/10.1029/2020JA028947

Harding, B. J., Gehrels, T. W., & Makela, J. J. (2014). Nonlinear regression method for estimating neutral wind and temperature from Fabry-Perot interferometer data. *Applied Optics*, *53*(4), 666–673. https://doi.org/10.1364/AO.53.000666

Harding, B. J., Ridley, A. J., & Makela, J. J. (2019). Thermospheric weather as observed by ground-based FPIs and modeled by GITM. *Journal of Geophysical Research: Space Physics*, *124*(2), 1307–1316. https://doi.org/10.1029/2018JA026032

Harding, B. J., Wu, Y.-J. J., Alken, P., Yamazaki, Y., Triplett, C. C., Immel, T. J., et al. (2022). Impacts of the January 2022 Tonga volcanic eruption on the ionospheric dynamo: ICON-MIGHTI and swarm observations of extreme neutral winds and currents. *Geophysical Research Letters*, *49*(9), e2022GL098577. https://doi.org/10.1029/2022GL098577

He, J., Astafyeva, E., Yue, X., Ding, F., & Maletckii, B. (2023). The giant ionospheric depletion on 15 January 2022 around the Hunga Tonga-Hunga Ha'apai volcanic eruption. *Journal of Geophysical Research: Space Physics*, *128*(1), e2022JA030984. https://doi.org/10.1029/2022JA030984

Heale, C. J., Inchin, P. A., & Snively, J. B. (2022). Primary versus secondary gravity wave responses at f-region heights generated by a convective source. *Journal of Geophysical Research: Space Physics*, *127*(1), e2021JA029947. https://doi.org/10.1029/2021JA029947

Hines, C. O. (1960). Internal atmospheric gravity waves at ionospheric heights. *Canadian Journal of Physics*, *38*(11), 1441–1481. https://doi.org/10.1139/p60-150

Horvath, A., Vadas, S., Stephan, C., & Buehler, S. (2023). One-minute resolution GOES-R observations of Lamb and gravity waves triggered by the Hunga Tonga-Hunga Ha'apai eruptions on 15 January 2022. *ESS Open Archive*. https://doi.org/10.22541/essoar.168565406.64574148/v1

Huba, J., Becker, E., & Vadas, S. (2023). Simulation study of the 15 January 2022 Tonga event: Development of super equatorial plasma bubbles. *Geophysical Research Letters*, *50*(1), e2022GL101185. https://doi.org/10.1029/2022GL101185

Hunt, B. R., Kostelich, E. J., & Szunyogh, I. (2007). Efficient data assimilation for spatiotemporal chaos: A local ensemble transform Kalman filter. *Physica D: Nonlinear Phenomena*, *230*(1), 112–126. (Data Assimilation). https://doi.org/10.1016/j.physd.2006.11.008

Inchin, P. A., Heale, C. J., Snively, J. B., & Zettergren, M. D. (2020). The dynamics of nonlinear atmospheric acoustic-gravity waves generated by tsunamis over realistic bathymetry. *Journal of Geophysical Research: Space Physics*, *125*(12), e2020JA028309. https://doi.org/10.1029/2020JA028309

Inchin, P. A., Heale, C. J., Snively, J. B., & Zettergren, M. D. (2022). Numerical modeling of tsunami-generated acoustic-gravity waves in mesopause airglow. *Journal of Geophysical Research: Space Physics*, *127*(8), e2022JA030301. https://doi.org/10.1029/2022JA030301

Inchin, P. A., Snively, J. B., Kaneko, Y., Zettergren, M. D., & Komjathy, A. (2021). Inferring the evolution of a large earthquake from its acoustic impacts on the ionosphere. *AGU Advances*, *2*(2), e2020AV000260. https://doi.org/10.1029/2020AV000260

Iwata, A., & Ishikawa, H. (1974). Lower ionospheric sounding by the use of Loran-C signals. *Journal of Geomagnetism and Geoelectricity*, *26*(5), 511–514. https://doi.org/10.5636/jgg.26.511

Ji, C., Wald, D. J., & Helmberger, D. V. (2002). Source description of the 1999 Hector Mine, California, earthquake, part I: Wavelet domain inversion theory and resolution analysis. *Bulletin of the Seismological Society of America*, *92*(4), 1192–1207. https://doi.org/10.1785/0120000916

Kanamori, H., & Given, J. W. (1981). Use of long-period surface waves for rapid determination of earthquake-source parameters. *Physics of the Earth and Planetary Interiors*, *27*(1), 8–31. https://doi.org/10.1016/0031-9201(81)90083-2

Khaykin, S., Podglajen, A., Ploeger, F., Grooß, J.-U., Tencé, F., Bekki, S., et al. (2022). Global perturbation of stratospheric water and aerosol burden by Hunga eruption. *Communications Earth & Environment*, *3*(1), 316. https://doi.org/10.1038/s43247-022-00652-x

Koch, S. E., & Saleeby, S. (2001). An automated system for the analysis of gravity waves and other mesoscale phenomena. *Weather and Forecasting*, *16*(6), 661–679. https://doi.org/10.1175/1520-0434(2001)016⟨0661:AASFTA⟩2.0.CO;2

Komjathy, A., Yang, Y.-M., Meng, X., Verkhoglyadova, O., Mannucci, A. J., & Langley, R. B. (2016). Review and perspectives: Understanding natural-hazards-generated ionospheric perturbations using GPS measurements and coupled modeling. *Radio Science*, *51*(7), 951–961. https://doi.org/10.1002/2015RS005910

Koshin, D., Sato, K., Miyazaki, K., & Watanabe, S. (2020). An ensemble Kalman filter data assimilation system for the whole neutral atmosphere. *Geoscientific Model Development*, *13*(7), 3145–3177. https://doi.org/10.5194/gmd-13-3145-2020

Kubota, T., Saito, T., & Nishida, K. (2022). Global fast-traveling tsunamis driven by atmospheric Lamb waves on the 2022 Tonga eruption. *Science*, *377*(6601), eabo4364. https://doi.org/10.1126/science.abo4364

Lamb, H. (1924). *Hydrodynamics*. University Press.

Laskar, F. I., Pedatella, N. M., Codrescu, M. V., Eastes, R. W., Evans, J. S., Burns, A. G., & McClintock, W. (2021). Impact of GOLD retrieved thermospheric temperatures on a whole atmosphere data assimilation model. *Journal of Geophysical Research: Space Physics*, *126*(1), e2020JA028646. https://doi.org/10.1029/2020JA028646

Le Pichon, A., Pilger, C., Ceranna, L., Marchetti, E., Lacanna, G., Souty, V., et al. (2021). Using dense seismo-acoustic network to provide timely warning of the 2019 paroxysmal Stromboli eruptions. *Scientific Reports*, *11*(1), 1–12. https://doi.org/10.1038/s41598-021-93942-x

Li, R., Lei, J., Kusche, J., Dang, T., Huang, F., Luan, X., et al. (2023). Large-scale disturbances in the upper thermosphere induced by the 2022 Tonga volcanic eruption. *Geophysical Research Letters*, *50*(3), e2022GL102265. https://doi.org/10.1029/2022GL102265

Lin, J.-T., Rajesh, P. K., Lin, C. C. H., Chou, M.-Y., Liu, J.-Y., Yue, J., et al. (2022). Rapid conjugate appearance of the giant ionospheric lamb wave signatures in the Northern Hemisphere after Hunga-Tonga volcano eruptions. *Geophysical Research Letters*, *49*(8), e2022GL098222. https://doi.org/10.1029/2022GL098222

Lindzen, R. S., & Blake, D. (1972). Lamb waves in the presence of realistic distributions of temperature and dissipation. *Journal of Geophysical Research*, *77*(12), 2166–2176. https://doi.org/10.1029/JC077i012p02166

Liu, C. H., Klostermeyer, J., Yeh, K. C., Jones, T. B., Robinson, T., Holt, O., et al. (1982). Global dynamic responses of the atmosphere to the eruption of Mount St. Helens on May 18, 1980. *Journal of Geophysical Research*, *87*(A8), 6281–6290. https://doi.org/10.1029/JA087iA08p06281

Liu, H.-L., Wang, W., Huba, J. D., Lauritzen, P. H., & Vitt, F. (2023). Atmospheric and ionospheric responses to Hunga-Tonga volcano eruption simulated by WACCM-X. *Geophysical Research Letters*, *50*(10), e2023GL103682. https://doi.org/10.1029/2023GL103682

Makela, J. J., Lognonné, P., Hébert, H., Gehrels, T., Rolland, L., Allgeyer, S., et al. (2011). Imaging and modeling the ionospheric airglow response over Hawaii to the tsunami generated by the Tohoku earthquake of 11 march 2011. *Geophysical Research Letters*, *38*(24), 165. https://doi.org/10.1029/2011GL047860

Makela, J. J., Meriwether, J., Ridley, A., Ciocca, M., & Castellez, M. (2012). Large-scale measurements of thermospheric dynamics with a multisite Fabry-Perot interferometer network: Overview of plans and results from midlatitude measurements. *International Journal of Geophysics*, *2012*, 1–10. https://doi.org/10.1155/2012/872140

Mannucci, A., Wilson, B., Yuan, D., Ho, C., Lindqwister, U., & Runge, T. (1998). A global mapping technique for GPS-derived ionospheric total electron content measurements. *Radio Science*, *33*(3), 565–582. https://doi.org/10.1029/97RS02707

Martire, L., Krishnamoorthy, S., Vergados, P., Romans, L. J., Szilágyi, B., Meng, X., et al. (2023). The GUARDIAN system-a GNSS upper atmospheric real-time disaster information and alert network. *GPS Solutions*, *27*(1), 1–13. https://doi.org/10.1007/s10291-022-01365-6

Matoza, R. S., Fee, D., Assink, J. D., Iezzi, A. M., Green, D. N., Kim, K., et al. (2022). Atmospheric waves and global seismoacoustic observations of the January 2022 Hunga eruption, Tonga. *Science*, *377*(6601), 95–100. https://doi.org/10.1126/science.abo7063

Millan, L., Santee, M. L., Lambert, A., Livesey, N. J., Werner, F., Schwartz, M. J., et al. (2022). Hunga Tonga-Hunga Ha'apai Hydration of the stratosphere. *Earth and Space Science Open Archive*. https://doi.org/10.1002/essoar.10511266.1

Munaibari, E., Rolland, L. M., Sladen, A., & Delouis, B. (2023). Anatomy of the tsunami and Lamb waves-induced ionospheric signatures generated by the 2022 Hunga Tonga volcanic eruption. *Pure and Applied Geophysics*, *180*(5), 1751–1764. https://doi.org/10.1007/s00024-023-03271-5

Nadolski, V. (1998). *Automated surface observing system (ASOS) user's guide* (p. 74). National Oceanic and Atmospheric Administration, Department of Defense, Federal Aviation Administration, United States Navy, 20. NOAA Tech. Report. Retrieved from http://www.nws.noaa.gov/asos/pdfs/aum-toc.pdf

Nishioka, M., Tsugawa, T., Kubota, M., & Ishii, M. (2013). Concentric waves and short-period oscillations observed in the ionosphere after the 2013 Moore EF5 tornado. *Geophysical Research Letters*, *40*(21), 5581–5586. https://doi.org/10.1002/2013GL057963

Ohminato, T., Chouet, B. A., Dawson, P., & Kedar, S. (1998). Waveform inversion of very long period impulsive signals associated with magmatic injection beneath Kilauea Volcano, Hawaii. *Journal of Geophysical Research*, *103*(B10), 23839–23862. https://doi.org/10.1029/98jb01122

Parkinson, B., Spilker, J., Axelrad, P., & Enge, P. (1995). Global positioning system: Theory and applications (Vol. *1*).

Paxton, L., Lewis, C. D., & Nayak, M. (2022). Understanding the ionospheric impact of the coupled system surface: DARPA's AtmoSense: Atmosphere as a sensor. In *AGU fall meeting*. Retrieved from https://agu.confex.com/agu/fm22/meetingapp.cgi/Paper/1051050

Peltier, W. R., & Hines, C. O. (1976). On the possible detection of tsunamis by a monitoring of the ionosphere. *Journal of Geophysical Research*, *81*(12), 1995–2000. https://doi.org/10.1029/JC081i012p01995

Picone, J. M., Hedin, A. E., Drob, D. P., & Aikin, A. C. (2002). NRLMSISE-00 empirical model of the atmosphere: Statistical comparisons and scientific issues. *Journal of Geophysical Research*, *107*(A12), SIA15-1–SIA15-16. https://doi.org/10.1029/2002JA009430

Pierce, A. D., & Posey, J. W. (1971). Theory of the excitation and propagation of Lamb's atmospheric edge mode from nuclear explosions. *Geophysical Journal International*, *26*(1–4), 341–368. https://doi.org/10.1111/j.1365-246X.1971.tb03406.x

Pilger, C., Gaebler, P., Hupe, P., Kalia, A. C., Schneider, F. M., Steinberg, A., et al. (2021). Yield estimation of the 2020 Beirut explosion using open access waveform and remote sensing data. *Scientific Reports*, *11*(1), 1–14. https://doi.org/10.1038/s41598-021-93690-y

Poli, P., & Shapiro, N. M. (2022). Rapid characterization of large volcanic eruptions: Measuring the impulse of the Hunga Tonga Ha'apai explosion from teleseismic waves. *Geophysical Research Letters*, *49*(8), e2022GL098123. https://doi.org/10.1029/2022GL098123

Pradipta, R., Carter, B. A., Currie, J. L., Choy, S., Wilkinson, P., Maher, P., & Marshall, R. (2023). On the propagation of traveling ionospheric disturbances from the Hunga Tonga-Hunga Ha'apai volcano eruption and their possible connection with tsunami waves. *Geophysical Research Letters*, *50*(6), e2022GL101925. https://doi.org/10.1029/2022GL101925

Press, F., & Harkrider, D. (1962). Propagation of acoustic-gravity waves in the atmosphere. *Journal of Geophysical Research*, *67*(10), 3889–3908. https://doi.org/10.1029/JZ067i010p03889

Rakoto, V., Lognonné, P., Rolland, L., & Coïsson, P. (2018). Tsunami wave Height estimation from GPS-derived ionospheric data. *Journal of Geophysical Research: Space Physics*, *123*(5), 4329–4348. https://doi.org/10.1002/2017JA024654

Savastano, G., Komjathy, A., Verkhoglyadova, O., Mazzoni, A., Crespi, M., Wei, Y., & Mannucci, A. J. (2017). Real-time detection of tsunami ionospheric disturbances with a stand-alone GNSS receiver: A preliminary feasibility demonstration. *Scientific Reports*, *7*(1), 1–10. https://doi.org/10.1038/srep46607

Shao, X.-M., & Lay, E. H. (2016). The origin of infrasonic ionosphere oscillations over tropospheric thunderstorms. *Journal of Geophysical Research: Space Physics*, *121*(7), 6783–6798. https://doi.org/10.1002/2015JA022118

Taylor, M., & Hapgood, M. (1988). Identification of a thunderstorm as a source of short period gravity waves in the upper atmospheric nightglow emissions. *Planetary and Space Science*, *36*(10), 975–985. https://doi.org/10.1016/0032-0633(88)90035-9

Themens, D. R., Watson, C., Žagar, N., Vasylkevych, S., Elvidge, S., McCaffrey, A., et al. (2022). Global propagation of ionospheric disturbances associated with the 2022 Tonga Volcanic Eruption. *Geophysical Research Letters*, *49*(7), e2022GL098158. https://doi.org/10.1029/2022GL098158

Titov, V. V., Gonzalez, F. I., Bernard, E., Eble, M. C., Mofjeld, H. O., Newman, J. C., & Venturato, A. J. (2005). Real-time tsunami forecasting: Challenges and solutions. *Natural Hazards*, *35*(1), 35–41. https://doi.org/10.1007/s11069-004-2403-3

Vadas, S. L., Becker, E., Figueiredo, C., Bossert, K., Harding, B. J., & Gasque, L. C. (2023a). Primary and secondary gravity waves and large-scale wind changes generated by the Tonga volcanic eruption on 15 January 2022: Modeling and comparison with ICON-MIGHTI winds. *Journal of Geophysical Research: Space Physics*, *128*(2), e2022JA031138. https://doi.org/10.1029/2022JA031138

Vadas, S. L., Figueiredo, C., Becker, E., Huba, J. D., Themens, D. R., Hindley, N. P., et al. (2023b). Traveling ionospheric disturbances induced by the secondary gravity waves from the Tonga eruption on 15 January 2022: Modeling with MESORAC-HIAMCM-SAMI3 and comparison with GPS/TEC and ionosonde data. *Journal of Geophysical Research: Space Physics*, *128*(6), e2023JA031408. https://doi.org/10.1029/2023JA031408

Vadas, S. L., Makela, J. J., Nicolls, M. J., & Milliff, R. F. (2015). Excitation of gravity waves by ocean surface wave packets: Upward propagation and reconstruction of the thermospheric gravity wave field. *Journal of Geophysical Research: Space Physics*, *120*(11), 9748–9780. https://doi.org/10.1002/2015JA021430

Vergoz, J., Hupe, P., Listowski, C., Le Pichon, A., Garcés, M., Marchetti, E., et al. (2022). IMS observations of infrasound and acoustic-gravity waves produced by the January 2022 volcanic eruption of Hunga, Tonga: A global analysis. *Earth and Planetary Science Letters*, *591*, 117639. https://doi.org/10.1016/j.epsl.2022.117639

Watanabe, S., Hamilton, K., Sakazaki, T., & Nakano, M. (2022). First detection of the Pekeris internal global atmospheric resonance: Evidence from the 2022 Tonga eruption and from global reanalysis data. *Earth and Space Science Open Archive*, *36*, 3027. https://doi.org/10.1002/essoar.10510971.1

Winn, S., Sarmiento, A., Alferez, N., & Touber, E. (2023). Two-way coupled long-wave isentropic ocean-atmosphere dynamics. *Journal of Fluid Mechanics*, *959*, A22. https://doi.org/10.1017/jfm.2023.131

Wright, C. J., Hindley, N. P., Alexander, M. J., Barlow, M., Hoffmann, L., Mitchell, C. N., et al. (2022). Surface-to-space atmospheric waves from Hunga Tonga-Hunga Ha'apai eruption. *Nature*, *609*(7928), 1–3. https://doi.org/10.1038/s41586-022-05012-5

Yuen, D. A., Scruggs, M. A., Spera, F. J., Zheng, Y., Hu, H., McNutt, S. R., et al. (2022). Under the surface: Pressure-induced planetary-scale waves, volcanic lightning, and gaseous clouds caused by the submarine eruption of Hunga Tonga-Hunga Ha'apai volcano. *Earthquake Research Advances*, *2*(3), 100134. https://doi.org/10.1016/j.eqrea.2022.100134

Zawdie, K., Belehaki, A., Burleigh, M., Chou, M.-Y., Dhadly, M. S., Greer, K., et al. (2022). Impacts of acoustic and gravity waves on the ionosphere. *Frontiers in Astronomy and Space Sciences*, *9*, 1064152. https://doi.org/10.3389/fspas.2022.1064152

Zedek, F., Rolland, L. M., Mikesell, T. D., Sladen, A., Delouis, B., Twardzik, C., & Coïsson, P. (2021). Locating surface deformation induced by earthquakes using GPS, GLONASS and Galileo ionospheric sounding from a single station. *Advances in Space Research*, *68*(8), 3403–3416. https://doi.org/10.1016/j.asr.2021.06.011

Zhang, J., Xu, J., Wang, W., Wang, G., Ruohoniemi, J. M., Shinbori, A., et al. (2022). Oscillations of the ionosphere caused by the 2022 Tonga volcanic eruption observed with SuperDARN radars. *Geophysical Research Letters*, *49*(20), e2022GL100555. https://doi.org/10.1029/2022GL100555

Zhang, S.-R., Vierinen, J., Aa, E., Goncharenko, L. P., Erickson, P. J., Rideout, W., et al. (2022). 2022 Tonga volcanic eruption induced global propagation of ionospheric disturbances via lamb waves. *Frontiers in Astronomy and Space Sciences*, *9*, 871275. https://doi.org/10.3389/fspas.2022.871275